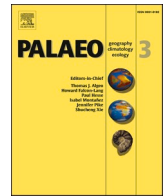




Contents lists available at ScienceDirect

Palaeogeography, Palaeoclimatology, Palaeoecology

journal homepage: www.elsevier.com/locate/palaeo

Carbonate shutdown, phosphogenesis and the variable style of marine anoxia in the late Famennian (Late Devonian) in western Laurentia

Sen Li^{a,*}, Paul B. Wignall^a, Simon W. Poulton^a, Makram Hedhli^c, Stephen E. Grasby^{b,c}^a University of Leeds, School of Earth and Environment, Leeds LS2 9JT, UK^b University of Calgary, Department of Geoscience, 2500 University Drive NW, Calgary, Alberta T2N 1N4, Canada^c Geological Survey of Canada, 3303-33rd Street NW, Calgary, Alberta T2L 2A7, Canada

ARTICLE INFO

Editor: Shucheng Xie

Keywords:

Carbonate demise
Framboidal pyrite
Exshaw Formation
Hangenberg Crisis
Black shale

ABSTRACT

The shutdown of carbonate productivity and its replacement by black shale deposition is often observed in the geological record and yet the factors driving such a change are debated. The latest Famennian of western Laurentia (present day North America) provides a good example of a limestone – black shale transition that is roughly contemporaneous with the global Hangenberg Crisis – a series of environmental and biotic changes associated with the widespread development of black shale deposition. However, in western Laurentia limestone deposition ceased and black shale deposition began prior to this crisis. Examining the type section of the Exshaw Formation at Jura Creek (Alberta) reveals that declining seafloor oxygen levels were likely responsible for the loss of carbonate productivity, followed by phosphogenesis of the youngest carbonates. The top surface of the limestone is a hard ground that was reworked, possibly by internal wave action, producing a lag of phosphatic clasts and pyrite grains including giant framboids (reaching 100 µm diameter) and polyframboids. The subsequent redox history of the lower Exshaw Formation shows substantial variations. Initially, the occurrence of small framboids, and elevated Fe_{HR}/Fe_T and Fe_{py}/Fe_{HR} combined with enhanced U, Mo and Re concentrations indicates intense euxinia in the water column. These conditions were replaced by ferruginous anoxic conditions recorded in radiolarian-rich black shales that have moderate concentrations of trace metals, and low pyrite content, as confirmed both by low Fe_{py}/Fe_{HR} ratios and scanning electron microscope (SEM) observation. Mo-U covariation trends suggest that Mo enrichment under ferruginous conditions was promoted by drawdown in association with Fe minerals precipitated in the water column. The return of better ventilated conditions around the Devonian/Carboniferous boundary is marked by a decrease in trace metal content and the loss of syngenetic pyrite. The Hangenberg Crisis is thus marked by an improvement in ventilation, from euxinic to ferruginous conditions in our study, and evidence from other basins in western North America suggests an even greater increase in oxygenation at this time.

1. Introduction

The demise of carbonate platforms can be due to a number of factors including the encroachment of siliciclastic sediment (e.g. Wilmsen, 2000) and salinity changes (e.g. Hornung et al., 2007). However, in many cases carbonates are overlain by a hiatal surface – suggesting little sediment influx – and black shales (e.g. Caplan et al., 1996; Petrash et al., 2016). In these circumstances it is tempting to explain the shutdown of carbonate productivity to the development of the anoxic environments in which black shales accumulate. This could either be driven by nutrient influx and elevated primary productivity or a change

in circulation regime and a decline in bottom water oxygen renewal. Often it is difficult to truly assess such shutdown mechanisms because the key evidence lies at a hiatal surface and so is associated with little or no sedimentary record. Here we address this issue with a detailed study of one such limestone-to-black shale transition: the boundary between the Palliser Formation carbonates and Exshaw Formation black shales from the latest Devonian of western Canada (cf. Johnston et al., 2010). This changeover was part of a widespread transition that encompasses the Hangenberg Crisis – an interval that also saw the widespread loss of carbonate deposition in Europe (Kaiser et al., 2016).

The latest Devonian was marked by major biotic and environmental

* Corresponding author.

E-mail address: eesli@leeds.ac.uk (S. Li).<https://doi.org/10.1016/j.palaeo.2022.110835>

Received 16 August 2021; Received in revised form 19 November 2021; Accepted 5 January 2022

Available online 10 January 2022

0031-0182/© 2022 The Authors. Published by Elsevier B.V. This is an open access article under the CC BY license (<http://creativecommons.org/licenses/by/4.0/>).

events, including a mass extinction, major sea-level oscillations linked to glaciation in the southern hemisphere, and widespread anoxia and shutdown of carbonate productivity (Becker, 1993; Walliser, 1996; Carmichael et al., 2016; Kaiser et al., 2016). This series of events is known as the Hangenberg Crisis, named after stratigraphic units in Germany (Fig. 1). The crisis began in the late Famennian following a brief sea-level fall around the end of the Lower *S. praesulcata* Zone (Fig. 1). This is thought to have been of glacioeustatic origin, and saw the Drewer Sandstone replace the Wocklum Limestone in Germany (Sandberg et al., 2002). Subsequent transgression and deepening in the early part of the Mid *praesulcata* Zone was associated with the spread of black shales, such as the Hangenberg Black Shale (Walliser, 1996; Caplan and Bustin, 1999; Kump et al., 2019). These organic-rich strata replaced limestones in many regions, with carbonate productivity generally being low throughout the Hangenberg Crisis. A contemporaneous, positive excursion in the $\delta^{238}\text{U}$ record suggests extensive U drawdown linked to the development of globally extensive anoxia (Zhang et al., 2020) for up to 80 kyr (Myrow et al., 2013). Deposition of

Hangenberg anoxic facies was terminated in the late Mid *praesulcata* Zone, either due to increased siliciclastic input producing the Hangenberg Sandstone, or by the development of marls and oolites (Fig. 1). Carbonate deposition only resumed in Europe with the Stockum Limestone (Fig. 1) in the Upper *praesulcata* Zone (Bábek et al., 2016).

Extensive black shales also occur in the Devonian-Carboniferous transitional strata in western North America, where they too overlie extensive carbonate deposits (Savoy, 1992; Smith et al., 1995; Savoy et al., 1999; Hart and Hofmann, 2018; Over, 2021). Similar to the European anoxic facies, there is much debate over the cause of this transition in North America. Regionally, two black shale units developed across several depocentres in the region (Fig. 1), specifically in the lower member of the Bakken Formation and the lower part of the Exshaw Formation (Smith and Bustin, 2000; Johnston et al., 2010). However, based on conodont biostratigraphy data it appears that black shale deposition began earlier than in Europe and persisted for longer (Johnston et al., 2010) (Fig. 1). It is thus unclear whether deposition of the Hangenberg black shales in Europe reflects a global intensification of

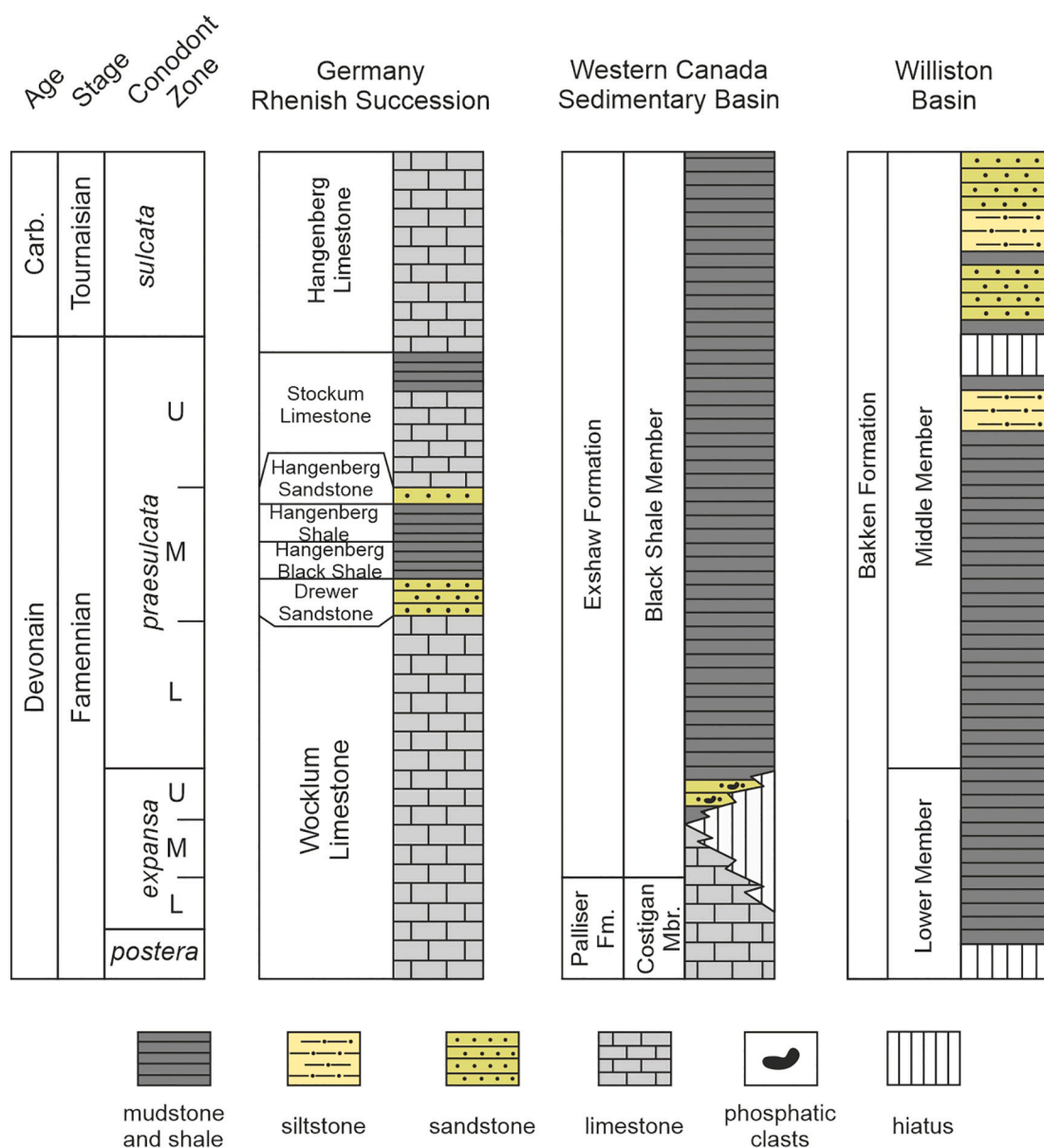


Fig. 1. Correlation of latest Devonian- earliest Carboniferous stratigraphy from the Western Canada Sedimentary Basin (Caplan and Bustin, 1999), Rhenish Basin, Germany (Kaiser et al., 2016) and Williston Basin, Montana, the Dakotas and the southern prairies of Canada (Smith and Bustin, 1998; Hogancamp and Pocknall, 2018). Mbr. =Member; Fm. =Formation; Carb. =Carboniferous.

anoxia driven by a unified driver (such as climate change or eustasy), or if it was a coincidence of local causes.

Links between glaciation and the development of Hangenberg anoxia include the possibility that enhanced circulation in cooler oceans may have led to increased nutrient supply and elevated productivity, thereby creating water column anoxia (Caplan and Bustin, 1999, 2001; Sageman et al., 2003; Bábek et al., 2016; Kumpan et al., 2019). In western North America factors, such as tectonism and the degree of basin isolation may provide an alternative explanation for the occurrence of the anoxic facies that are only partly contemporaneous with the Hangenberg Crisis. The notion that limited circulation in semi-isolated basins was responsible for black shale deposition is supported by geochemical proxies for restriction (Richard et al., 2002; Algeo et al., 2007). However, other researchers favour a model in which eustatic transgression and deepening allowed oceanic nutrients to invade the North American epicontinental basins, fostering high productivity and black shale development (Savoy, 1992; Smith and Bustin, 1998; Caplan and Bustin, 1999, 2001). These debates also link to discussion on the water depth at which black shales form: some models envisage black shales forming in shallow lagoons beneath a stratified water column (Raasch, 1956; Petty, 2019), while others favour deposition beneath hundreds of metres of water (Webster, 1984; Savoy, 1992; Smith and Bustin, 1998).

Explaining the origin of a thin, phosphatic sandstone bed found at the base of the Exshaw Formation black shale (Fig. 1) may help in understanding why carbonate deposition was replaced with black shale accumulation. The phosphate-rich level has been attributed to four alternative circumstances: 1) as a result of a regression that terminated carbonate production prior to onlap and black shale development (Smith et al., 1995); 2) as a product of eutrophication that elevated primary productivity and caused the demise of carbonate production (Caplan et al., 1996); 3) as a storm deposit formed after carbonate shut down (Richards and Higgins, 1988; Egenhoff and Fishman, 2013); or 4) as a lag deposit formed by dissolution of underlying carbonate as a deep-water chemocline transgressed over a carbonate ramp (Caplan and Bustin, 1999, 2001). These scenarios all have very different implications for the cause of carbonate shut-down and black shale development.

In order to investigate these debates, we have undertaken an integrated petrographic and geochemical study of sedimentary facies and redox changes at the type location of the Exshaw Formation's lower member in western Alberta, Canada. We aim to assess how redox conditions evolved and how they may have contributed to carbonate deposition shutdown.

2. Regional geology

Important and much debated tectonic events associated with the Antler Orogeny occurred in western North America during the Late Devonian – Early Carboniferous (Root, 2001). There were several major depocentres in western Laurentia most notably the hydrocarbon-rich Williston Basin (Richards and Higgins, 1988; Hogancamp and Pocknall, 2018; Hart and Hofmann, 2018). This straddled the United States/Canadian border and is found in present day North Dakota, South Dakota, easternmost Montana, and southern Saskatchewan and saw the deposition of the Bakken Formation. The lower member records the development of anoxic-euxinic conditions in the late Famennian *postera* – *praesulcata* zonal interval and was succeeded by a more heterolithic, burrowed, middle member following a short hiatus around the Devonian-Carboniferous boundary (Fig. 1) (Smith and Bustin, 2000; Egenhoff, 2017; Hogancamp and Pocknall, 2018). This in turn is overlain by another argillaceous unit, the Upper Bakken black shale, that records anoxic-dysoxic conditions (Borcovsky et al., 2017). West of the Williston Basin, in Montana, the Sappington Basin also contains a Devonian-Carboniferous black shale unit, the Sappington Formation (di Pasquo et al., 2019; Browne et al., 2020). Like the Bakken Formation, the Sappington black shales occur as two separate members separated by more oxygenated facies developed during the Devonian-Carboniferous

boundary interval.

A separate depocentre, the Western Canada Sedimentary Basin, was also the locus of deposition of two black shale units separated by an organic-poor siltstone (Caplan and Bustin, 1999; Smith and Bustin, 2000; Johnston et al., 2010; Over, 2021). In this region, a Black Shale Member of the Exshaw Formation overlies carbonates of the Palliser Formation (Fig. 2), with a hiatus spanning up to three conodont Zones at the contact (Johnston et al., 2010). The conodont fauna of the Exshaw Formation indicates that the onset of black shale deposition began in the earlier part of the *expansa* Zone (Richards et al., 1994; Johnston et al., 2010). This is roughly contemporaneous with the onset of black shale deposition in the adjacent Williston Basin although it clearly predates Hangenberg anoxia in western Europe (Fig. 1). However, anoxic deposition persisted into the Carboniferous in the Western Canada Sedimentary Basin and the upper part of the Black Shale Member thus records the Hangenberg Event.

Our study focusses on the type section of the Exshaw Formation at Jura Creek, a tributary to the Bow River, western Alberta (Richards and Higgins, 1988; Richards et al., 1994; Fig. 2). A thin, phosphatic sandstone, of highly debated origin (see above), separates carbonates of the upper Costigan Member of the Palliser Formation from the overlying black shales of the Exshaw Formation (Fig. 2). The phosphatic sandstone is overlain by nearly 10 m of black shale that becomes calcareous in the upper third. Conodonts indicate that the lower, non-calcareous black shales belong to the lower part of the *expansa* Zone, with the central part ranging to the upper *praesulcata* zones, whilst the Devonian-Carboniferous boundary occurs within a ~ 4 m-thick interval (Richards and Higgins, 1988; Richards et al., 1994; Over, 2021; Fig. 2).

3. Methods

3.1. Sample preparation and optical microscopy

A total of 21 shale and carbonate samples were collected from the Jura Creek section (Fig. 2). Minor weathered surfaces were removed and samples with visible signs of alteration and/or veining were rejected at this point. An agate mortar was used to crush samples into homogeneous powder (< 60 µm) for geochemical analyses. Microfacies analyses of carbonates and shales were also performed via petrographic microscopy and SEM. Nineteen polished blocks of around 5 cm² were prepared, coated in carbon, and examined using a TESCAN VEGA3 SEM under backscatter mode.

3.2. Major elements

Total organic carbon (TOC) analyses were determined on a LECO Carbon-Sulfur analyzer. Samples were de-carbonated prior to analysis using 50 vol% HCl. Replicate analyses of certified reference material (Soil LCRM with carbon content of 10.8 ± 0.26 wt%) gave a relative standard deviation (RSD) of 1%, and accuracy was ensured by analyses within 1% of reported values. Other major and trace elements were analysed following a total dissolution (Alcott et al., 2020). After ashing at 550 °C for 8 h, samples were quantitatively digested using concentrated HNO₃, HF and HClO₄, and left to dry before addition of H₃BO₃ to prevent the formation of Al complexes. Finally, the residues were redissolved with near-boiling HNO₃ and diluted with ultrapure 18 MΩ H₂O prior to analysis by ICP-OES (major elements) and ICP-MS (trace elements). Accuracy and precision, estimated from repeat analyses of USGS (United State Geological Survey) standard SGR-1b (Green River Shale), were better than 5%. Enrichment factors (EF) were used to assess the behaviour of Mo, U, V and Re in siliciclastic intervals (i.e. carbonates from unit 1 and the phosphatic sandstone from unit 2 were excluded), where $EF = (\text{metal}/\text{Al})_{\text{sample}}/(\text{metal}/\text{Al})_{\text{AUC}}$, and AUC represents average upper crust (McLennan, 2001).

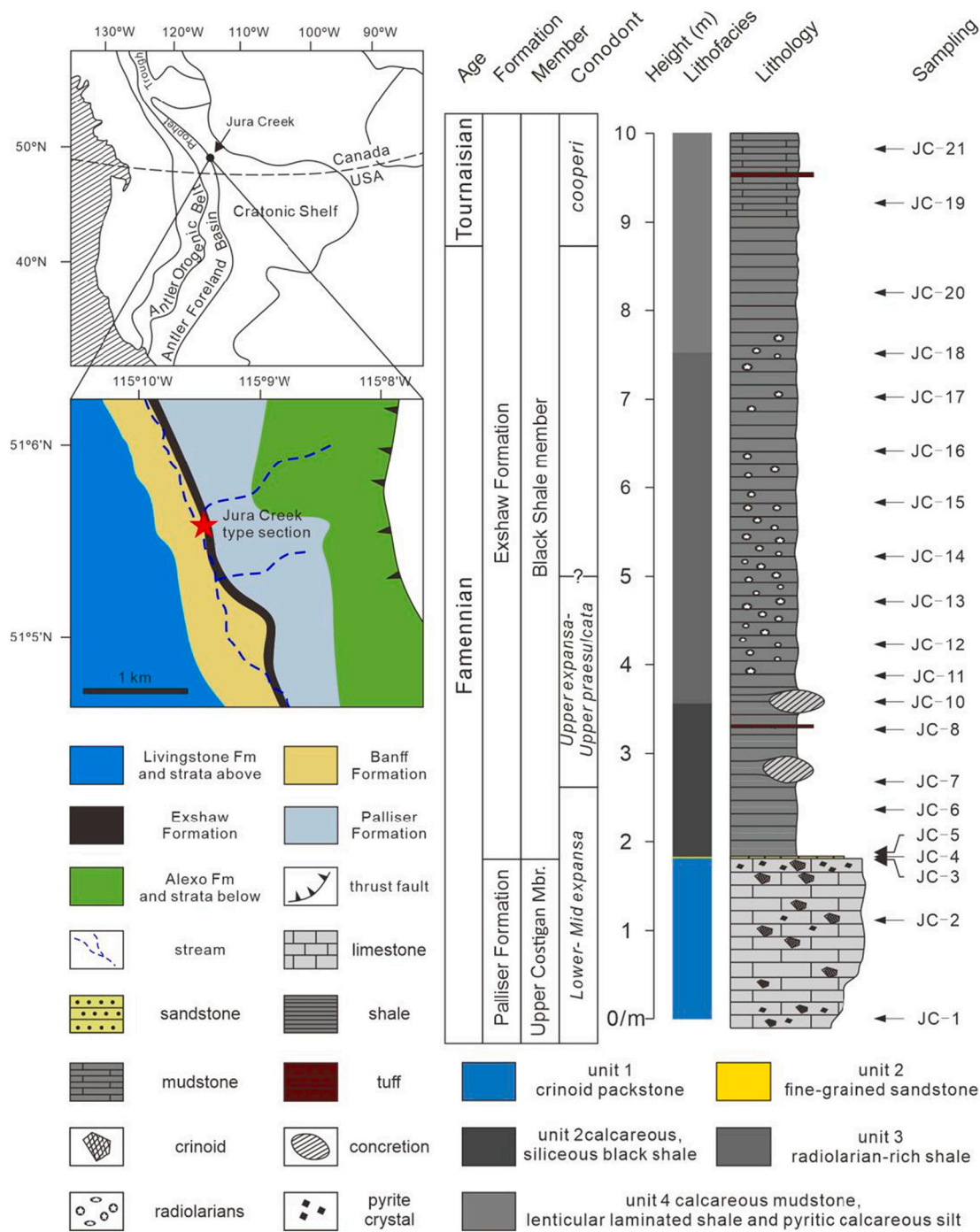


Fig. 2. Location of studied outcrop, stratigraphic log of the Jura Creek section and sample horizons. A simplified lithofacies column is introduced and used in the following figures. The approximate position of the Famennian-Tournaisian boundary is defined by Re- Os dating (Selby and Creaser, 2005).

3.3. Fe speciation

Sequential Fe extractions were performed according to the technique of Poulton and Canfield (2005). The procedure targets different operationally-defined Fe pools that are considered highly reactive (Fe_{HR}) towards dissolved sulphide in anoxic surface environments (Raiswell and Canfield, 1998; Poulton and Canfield, 2005; Poulton, 2021). The first step targets carbonate-associated iron (Fe_{carb}) via a 1 M sodium acetate extraction performed at pH 4.5 and 50 °C for 48 h. This was followed by a sodium dithionite extraction (2 h at room temperature), which targets Fe (oxyhydr)oxide minerals (Fe_{ox}). Finally, a 0.2 M ammonium oxalate/0.17 M oxalic acid solution was used (6 h at room

temperature) to target magnetite (Fe_{mag}). The concentration of Fe phases was determined using a Thermo Scientific iCE-3000 series flame atomic absorption spectrometer. Acid volatile sulphide (AVS) and pyrite (Fe_{py}) were determined on a separate sub-sample via a two-step chromous chloride distillation (Canfield et al., 1986), with the liberated sulphide trapped as Ag_2S and concentrations of sulphide determined gravimetrically. Replicate extractions of an international reference material (WHIT; Alcott et al., 2020) gave a RSD of <5% for each Fe pool, with analyses within 2% of reported values.

AVS was present at very low concentration in four samples, with only one sample (JC-4) containing a high concentration (Table 1). Sample JC-4 is a sandstone within the phosphatic horizon and has a high Zn

Table 1
Geochemical data for the Jura Creek samples.

Unit	Sample	Height (m)	TOC (wt%)	Fe _{carb} (wt%)	Fe _{ox} (wt%)	Fe _{mag} (wt%)	Fe _{py} (wt%)	AVS (wt%)	Fe _T (wt %)	Al (wt %)	P (ppm)	Mo (ppm)	U (ppm)	V (ppm)	Re (ppb)	Zn (ppm)
4	JC-21	9.82	0.22	0.59	0.02	0.02	1.18	0.03	1.96	2.95	420.4	0.79	1.12	58.69	14.59	10.57
	JC-19	9.22	0.65	0.75	0.04	0.02	1.52	0.05	2.37	3.75	482.0	3.47	2.04	69.92	4.65	31.34
	JC-20	8.22	1.77	0.44	0.06	0.02	2.57	0.00	3.68	7.66	523.2	7.70	2.39	221.1	12.64	76.20
	JC-18	7.52	3.81	0.04	0.37	0.02	0.15	0.00	0.81	5.58	89.00	53.80	10.23	1122	60.51	124.8
	JC-17	7.02	4.36	0.07	0.55	0.02	0.14	0.00	1.27	7.21	128.1	78.20	11.38	1576	83.34	188.5
	JC-16	6.42	4.19	0.18	0.73	0.02	0.15	0.00	1.36	5.28	192.6	69.51	10.77	1289	49.68	183.8
	JC-15	5.82	4.44	0.03	0.31	0.02	0.16	0.00	0.82	5.6	68.03	69.53	10.61	1400	71.78	65.79
3	JC-14	5.22	4.36	0.03	0.39	0.03	0.09	0.00	0.72	3.62	81.00	79.24	9.72	1167	31.95	93.68
	JC-13	4.72	3.91	0.02	0.24	0.02	0.12	0.00	0.58	3.29	107.2	74.03	8.09	1093	39.86	73.56
	JC-12	4.22	3.60	0.05	0.22	0.01	0.09	0.00	0.56	3.76	57.42	39.82	9.25	1205	28.35	35.56
	JC-11	3.87	4.20	ND	ND	ND	ND	ND	0.21	3.00	LQD	53.55	6.51	1147	34.98	26.74
	JC-10	3.57	3.48	0.07	0.84	0.02	0.16	0.00	1.31	3.86	330.1	72.12	13.49	1466	37.88	240.2
	JC-8	3.27	4.04	0.23	0.30	0.01	1.84	0.00	2.86	4.26	513.7	141.6	30.36	1855	174.2	153.6
	JC-7	2.67	4.15	0.11	0.14	0.01	0.58	0.00	1.04	3.78	106.4	53.15	13.07	479.2	34.03	17.39
2	JC-6	2.37	5.11	0.22	0.16	0.01	1.30	0.00	1.97	4.16	259.2	79.59	20.15	386.0	31.14	17.56
	JC-5	1.87	4.00	0.63	0.01	0.01	2.65	0.00	3.12	3.22	375.5	76.59	22.57	173.1	61.23	227.9
	JC-4	1.82	0.61	0.96	0.02	0.02	9.00	1.23	9.22	3.15	12,090	199.6	31.57	16.47	1065	227,374
	JC-3	1.8	0.12	0.38	0.03	0.01	6.54	0.07	6.8	0.65	1075	3.71	11.22	10.86	16.95	250.3
1	JC-2	1.1	0.10	ND	ND	ND	ND	ND	0.28	0.38	179.2	2.40	0.78	5.46	6.65	12.97
	JC-1	0	0.07	ND	ND	ND	ND	ND	0.43	0.76	244.8	0.19	0.35	8.87	3.67	5.67

TOC = total organic carbon, AVS. = acid-volatile sulphide, ND = not determined, LQD = limit of quantification.

concentration (Table 1), with petrographic observations demonstrating that much of this Zn is in the form of ZnS (which would be dissolved during the AVS extraction) (see *Pyrite petrography* section). Thus, we assign the AVS in this sample to ZnS, rather than FeS. For consistency, we also consider the minor AVS present in the four samples with low concentrations to dominantly reflect metal sulphides other than FeS. Note, however, that for these four samples, the low AVS concentrations mean that our results are unaffected by whether we assign the AVS to FeS or to other metal monosulphides. Given these considerations, we hereon define Fe_{HR} as the sum of Fe_{carb} + Fe_{ox} + Fe_{mag} + Fe_{py} (Poulton et al., 2004; Poulton and Canfield, 2011).

3.4. Framework for redox interpretations

We have combined three independent approaches for reconstructing water column and porewater redox conditions during deposition of the Jura Creek succession: pyrite framboid petrography, Fe speciation and trace metal systematics. Pyrite framboid sizes have been widely utilized to diagnose redox condition, especially euxinic (anoxic, sulfidic water column) conditions (Wilkin et al., 1996; Wilkin and Barnes, 1997; Wignall and Newton, 1998; Wignall et al., 2010). In modern euxinic environments framboids form in the water column and only achieve a small size with narrow distribution (Wilkin et al., 1996), whereas framboids can grow larger and are accompanied by higher proportions of diagenetic pyrite in dysoxic conditions (Wilkin and Arthur, 2001; Wignall et al., 2010).

We also use Fe speciation (Poulton and Canfield, 2005) to provide more detailed insight into the redox state of the water column. This technique is used to distinguish oxic, ferruginous (anoxic, Fe-containing) and euxinic water column conditions, whereby ratios of Fe_{HR} normalized to total Fe (Fe_T) < 0.22 suggest an oxic water column and Fe_{HR}/Fe_T ratios > 0.38 suggest anoxic water column conditions (Raiswell and Canfield, 1998; Raiswell et al., 2001; Poulton and Raiswell, 2002). Ratios of 0.22–0.38 are considered to be equivocal (Poulton and Canfield, 2011; Poulton, 2021). For samples deposited under anoxic water column conditions, Fe_{py}/Fe_{HR} ratios are used to distinguish euxinic from ferruginous conditions, whereby Fe_{py}/Fe_{HR} > 0.8 suggests euxinia, ratios of 0.6–0.8 are considered to potentially reflect euxinic depositional conditions, and Fe_{py}/Fe_{HR} < 0.6 implies ferruginous water column conditions (Poulton et al., 2004; Poulton and Canfield, 2011; Benkovitz et al., 2020; Poulton, 2021).

The different, redox-dependent behaviour of Mo, U, V and Re provides further insight into redox conditions. Molybdenum is delivered to the ocean as the largely unreactive molybdate anion (MoO₄²⁻), and under oxic conditions may be removed to the sediments (generally at low concentration) through uptake by Fe–Mn (oxyhydr)oxide minerals at the sea bed (Bertine and Turekian, 1973). Under ferruginous conditions, extensive water column precipitation of Fe minerals such as Fe (oxyhydr)oxides or green rust (e.g. Zegeye et al., 2012) may draw down higher concentrations of Mo through a particulate shuttle mechanism (e.g. Algeo and Tribouillard, 2009; Tribouillard et al., 2012). By contrast, when a critical threshold of free H₂S is met under euxinic conditions, the molybdate anion is converted to particle-reactive thiomolybdate (Helz et al., 1996), commonly resulting in significant Mo enrichment in the sediments (Emerson and Huested, 1991; Helz et al., 1996; Erickson and Helz, 2000).

Uranium reduction primarily occurs in anoxic sediments rather than in the water column, and U is therefore enriched beneath anoxic bottom waters, regardless of whether euxinic or ferruginous conditions dominate (Anderson et al., 1989; Klinkhammer and Palmer, 1991; Partin et al., 2013). By contrast, vanadium is commonly incorporated into sediments as the vanadate ion (H₂V(V)O₄⁻) adsorbed onto Mn oxides, and may be released from sediments during Mn oxide reduction under dysoxic porewater conditions (Emerson and Huested, 1991; Nameroff et al., 2002). Under anoxic conditions, however, the vanadate released following Mn oxide reduction is reduced to the vanadyl ion (V(IV)O₂⁺), which is highly surface-reactive and tends to be retained in the sediment (Emerson and Huested, 1991).

Rhenium is efficiently sequestered in the sediment under both euxinic and ferruginous conditions, as well as under dysoxic conditions when O₂ penetrates < 1 cm below the sediment–water interface (Crusius et al., 1996; Morford and Emerson, 1999). This specific behaviour has led to the use of elevated Re/Mo ratios as an indicator of dysoxic conditions at the sediment–water interface (e.g. Kendall et al., 2010; Schobben et al., 2020), which is predicated on the fact that Mo enrichments only occur under fully anoxic conditions, either through drawdown of particle-reactive thiomolybdate in the presence of dissolved sulphide (Emerson and Huested, 1991; Helz et al., 1996; Erickson and Helz, 2000), or via the particulate shuttle mechanism outlined above (Algeo and Tribouillard, 2009; Tribouillard et al., 2012). However, in the absence of a strong particulate shuttle for Mo under fully anoxic conditions, which would be typical of an anoxic, non-sulphidic

setting where the precipitation and depositional flux of Fe minerals from the water column was not high, elevated Re/Mo ratios would potentially occur under anoxic, as well as dysoxic, water column conditions. Given that this particular scenario was likely a common feature of ancient anoxic, non-sulphidic (commonly ferruginous) marine environments, where large expanses of the sea floor constituted a source of Fe^{2+} to the water column, rather than being a sink for Fe_{HR} minerals (Poulton, 2021; Poulton and Canfield, 2011), we here consider the additional use of Re/U ratios. Re/U ratios have the potential to provide more robust insight into the development of dysoxic conditions in the water column and at the sediment-water interface, since sequestration of U only requires anoxic porewater conditions (Anderson et al., 1989; Klinkhammer and Palmer, 1991), and hence dysoxic conditions will specifically be characterized by elevated Re/U.

4. Results

4.1. Lithofacies

Based on petrological examination, we have divided the Jura Creek section into four informal units (Fig. 2). The first/lowest unit consists of limestone of the Costigan Member (at 0–1.87 m); the second includes a 10 cm-thick, phosphatic, sandstone bed at the base, as well as an overlying calcareous and siliceous black shale (1.87–3.57 m) of the basal Exshaw Formation, which contains large carbonate concretions (Fig. 2); the third unit is a siliceous (radiolarian-rich) shale (3.57–7.52 m) with concretions at the base; the fourth unit consists of lenticular-laminated shale, calcareous mudstone and pyritic calcareous silt (7.52–9.82 m).

Within these four units we define seven lithofacies based on petrographic observations (Table 2). The first unit is dominated by crinoidal packstone (Fig. 3a; Facies 1). Other than crinoid columnals, other bioclasts include ophiuroid fragments and echinoid spines (Fig. 3a, c). In the uppermost bed of unit 1 (sample JC-3) the crinoidal packstone also contains intraclasts of rounded wackestone, around 1 cm in diameter (Fig. 4a, b), and shows heterogenous distributed bioclasts (Fig. 3b, c). Extensive pyrite replacement occurs in the uppermost bed especially of

echinoderm grains (Figs. 3d, 4a). Siliceous replacement was also observed in two forms: abundant dark, chert concretions in the topmost limestone, and chalcedonic quartz infilling voids within bioclasts (Fig. 4c, d).

The thin, phosphatic sandstone bed (sample JC-4; Facies 2) separating the Costigan Member and the Exshaw black shale consists of three distinct layers (Fig. 5a). A lower carbonate layer (L1) consists of irregular shaped (possibly abraded) fragments of echinoderms in a fine dolomitic matrix (Fig. 5b). The overlying layer (L2), a phosphatic sandstone, is dominated by angular, fine sand-size grains of quartz and feldspar, plus phosphate and pyrite grains (Fig. 5b). The contact between L1 and L2 is sharp, although sand grains are intermixed with dolomite rhombs at the transition, indicating that L1 was not lithified prior to deposition of L2 (Fig. 5c). Within L2, rounded phosphate clasts, up to 1.5 cm in length, are also seen (Fig. 5a). These contain bioclast fragments (replaced by pyrite) suggesting that they are phosphatised limestone clasts (Fig. 6f). Apart from the phosphatised clasts, L2 is dominated by sand grains and pyrite polyframboids and has a calcite cement. In the upper layer (L3), the cement is dominated by pyrite (Figs. 5d, 6b), except in the topmost part where calcite cement again occurs (Fig. 5e). L3 contains quartz, feldspar, pyrite polyframboids and phosphate clasts, similar to those in L2, together with elongate and curved phosphate grains that are likely fish ribs (Fig. 5e).

The petrography of the Black Shale Member shows a clear vertical evolution. The onset of calcareous black shale (Facies 3) in the second unit is marked by alternating laminations of organic-rich clay and calcisilt (Fig. 7a). The latter laminae range from 20 to 70 μm thickness and show horizontal persistence and low amplitude current ripples. Higher in the second unit, the calcite content declines whilst the siliceous content, in the form of scattered silt-grade quartz, increases (Fig. 7b, Facies 4). The third unit marks the transition to radiolarian-rich black shale, containing compacted radiolarian tests in a dark, organic-rich matrix that lacks lamination (Fig. 7c, Facies 4). The fourth unit consists of lenticular-laminated shale consisting of compacted clay clasts (Fig. 7d, Facies 5), calcareous mudstone bearing tiny shell fragments and ophiuroid ossicles (Fig. 7e, Facies 6), and pyrite-rich, calcisilt laminae

Table 2

Lithofacies, defined by petrographic features, and their interpreted environmental conditions from the Jura Creek section.

Lithofacies No.	Lithofacies	Petrological description	Dominant clasts	Mineral composition	Distribution	Pyrite content	Environmental Interpretation
1	Crinoidal packstone	Bioclasts and micrite matrix	Echinoderms, calcisphere and ophiuroid (Fig. 3a, c)	Mainly calcite, some pyrite and chert replacement	Topmost part of Costigan Member (JC-1 to JC-3)	Lower content in JC-1 and JC-2 but high in JC-3	Mid-ramp
2	Phosphatic sandstone	Grained supported with pyrite and calcite cement	Quartz, feldspar and pyrite, phosphatised clasts and bone fragments (Fig. 5)	Quartz, feldspar, phosphate, pyrite and calcite cement	Basal bed of Lower Exshaw Shale Member (JC-4)	Abundant pyrite both as cement, giant framboids and polyframboids	Transgression lag in a mid-ramp setting
3	Black calcareous shale	Laminae of clay-rich and calcite-rich layers with organic matter	Mostly clay-grade sediment but with calcite microcrystals (Fig. 7a)	Clay, calcite and pyrite	Basal part of Lower Exshaw Shale (JC-5)	Abundant small framboids	Euxinic, basinal setting
4	Black siliceous shale	scattered silty quartz or radiolarian	Mostly clay-grade sediment but with radiolarians, and silt-grade quartz, (Fig. 7b, c)	Clay, silica and pyrite	Middle and upper part of the Lower Exshaw Shale (JC-6 to JC-8; JC-10 to 18)	Some samples have abundant small framboids, other samples are pyrite free	euxinic bottom waters but pyrite-free samples recording ferruginous conditions, all in a basinal setting
5	Lenticular laminated shale	Thin beds and lenticular laminae consisting of flattened lenses of clay clasts	Mostly clay-grade sediment but with silt-grade quartz (Fig. 7d)	Clay, silica and pyrite	Upper part of Lower Exshaw Shale (JC-20)	Common pyrite, in form of both euhedral crystals and framboids	Dysoxic bottom waters with sulfidic sediment
6	Calcareous mudstone	Well-sorted calcite grains with small amount of bioclasts	Ophiuroid, bivalves and calcite microcrystal (Fig. 7e)	Clay and calcite	Top part of section (JC-19)	Common pyrite, in form of both euhedral crystals and framboids	Dysoxic bottom waters with sulfidic sediment
7	Pyritic calcareous silt	Well-sorted sand grains (calcite crystal)	Calcite microcrystal (Fig. 7f)	Calcite, pyrite	Top part of section (JC-21)	Rare pyrite, mainly occurs as scattered crystals	Weakly dysoxic bottom waters with sulfidic sediment

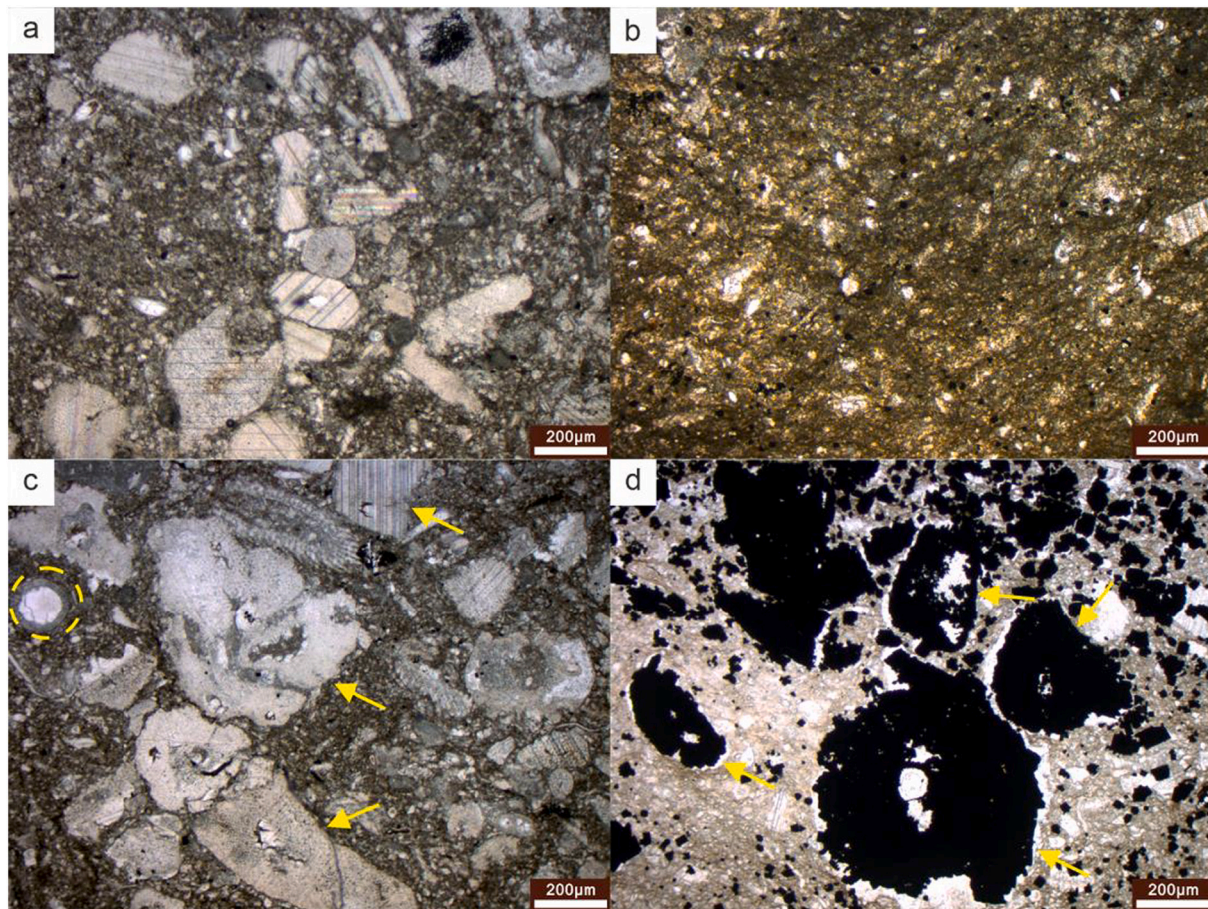


Fig. 3. Petrographic features of limestone in the Jura Creek section. (a) sample JC-2: packstone consisting of abundant bioclasts, mostly from echinoderm, within calcium mud matrix; (b) sample JC-3: middle part of limestone (see “f” area in Fig. 4a), packstone bearing limited bioclasts, bioclastic wackestone; (c) sample JC-3: bottom part of limestone (see “e” area in Fig. 4a), packstone bearing crinoid fragments (yellow arrows) and calcisphere (yellow circle); (d) sample JC-3: top part of limestone (see “g” area in Fig. 4a) showing crinoid fragments selectively replaced by pyrite (yellow arrows). (For interpretation of the references to colour in this figure legend, the reader is referred to the web version of this article.)

(Fig. 7f, Facies 7).

4.2. Pyrite petrography

SEM analysis reveals that pyrite crystals are common in the topmost bed of the Costigan Member (JC-3) (Fig. 6a) and overlying phosphatic sandstone (JC-4), where it also occurs as a cement (Fig. 6b). Framboidal pyrite occurs in the second and fourth units (Fig. 8), where their sizes were measured (Table 3; Fig. 9), but framboidal pyrite was not present in the Costigan limestone nor in unit 3 (with the exception of sample JC-17). Within the phosphatic sandstone, exceptionally large frambooids, up to 100 µm in diameter, were seen (Fig. 6e). These had large constituent microcrysts reaching up to 10 µm. Both of these dimensions are an order of magnitude larger than typical frambooids (Wignall and Newton, 1998). The large frambooids occur alongside equally large, composite, spherical grains of pyrite, around 80–100 µm in diameter, that resemble polyframbooids. However, unlike typical polyframbooids, which consist solely of spherical clusters of frambooids (Love, 1971; Love and Vanguetaine, 1973; Wei et al., 2016), the polyframbooids in JC-4 are composed of both frambooids and a range of other components; predominantly pyrite microcrysts, a few microns in size, that form the matrix between the frambooids (Fig. 6c), together with larger pyrite crystals (5–10 µm in size) and, in some cases, patches of sphalerite cement (Fig. 6d). The margins of the near-perfectly spherical grains are sharp, with frambooids at the outer edge of the polyframbooid being truncated (Fig. 6c). More ovoid polyframbooids (Fig. 6d) also occur

(possibly due to compaction) together with concentrations of frambooids with more diffuse boundaries that may be partially disintegrated polyframbooids or examples caught at the moment of coalescing.

The frambooids in unit 2 are small, with a mean diameter of ~4 µm, and they occur with small pyrite crystals (Fig. 8a), although one sample (JC-7) lacked frambooids (Fig. 9). Unusually for a black shale, samples of unit 3 lack frambooids or indeed any form of visible pyrite (JC-11 to JC-15, and JC-17). Only at the top of the unit do a limited amount of frambooids re-appear (sample JC-16, JC-18), together with common pyrite crystals. The pyrite content of unit 4 is dominated by euhedral crystals, although frambooids are also common (Fig. 8b). Minor, secondary overgrowth of crystalline pyrite is common on frambooid margins, although their central cores are still clear (Fig. 8c).

Plotting the frambooids’ mean diameter versus standard deviation (Fig. 9) shows that they mostly fall in the field typical of frambooids from modern euxinic environments (Wilkin et al., 1996). In the phosphatic sandstone, the diameter of the frambooids found within the polyframbooids was measured separately to the isolated frambooids found within the matrix (Table 3). The frambooids found in the polyframbooids (samples JC-4-1, JC-4-2) display a similar average size with a narrow size distribution, and plot close to the euxinic-dysoxic/oxic boundary in the size-standard deviation plot (Fig. 9). By contrast, the frambooids in sandstone matrix (JC-4-3) are considerably larger in size and show a broader size distribution, and thus plot in the dysoxic/oxic field (Fig. 9). The frambooids in the black shale of unit two (and the single, frambooid-bearing sample from unit 3) have a small size and narrow distribution,

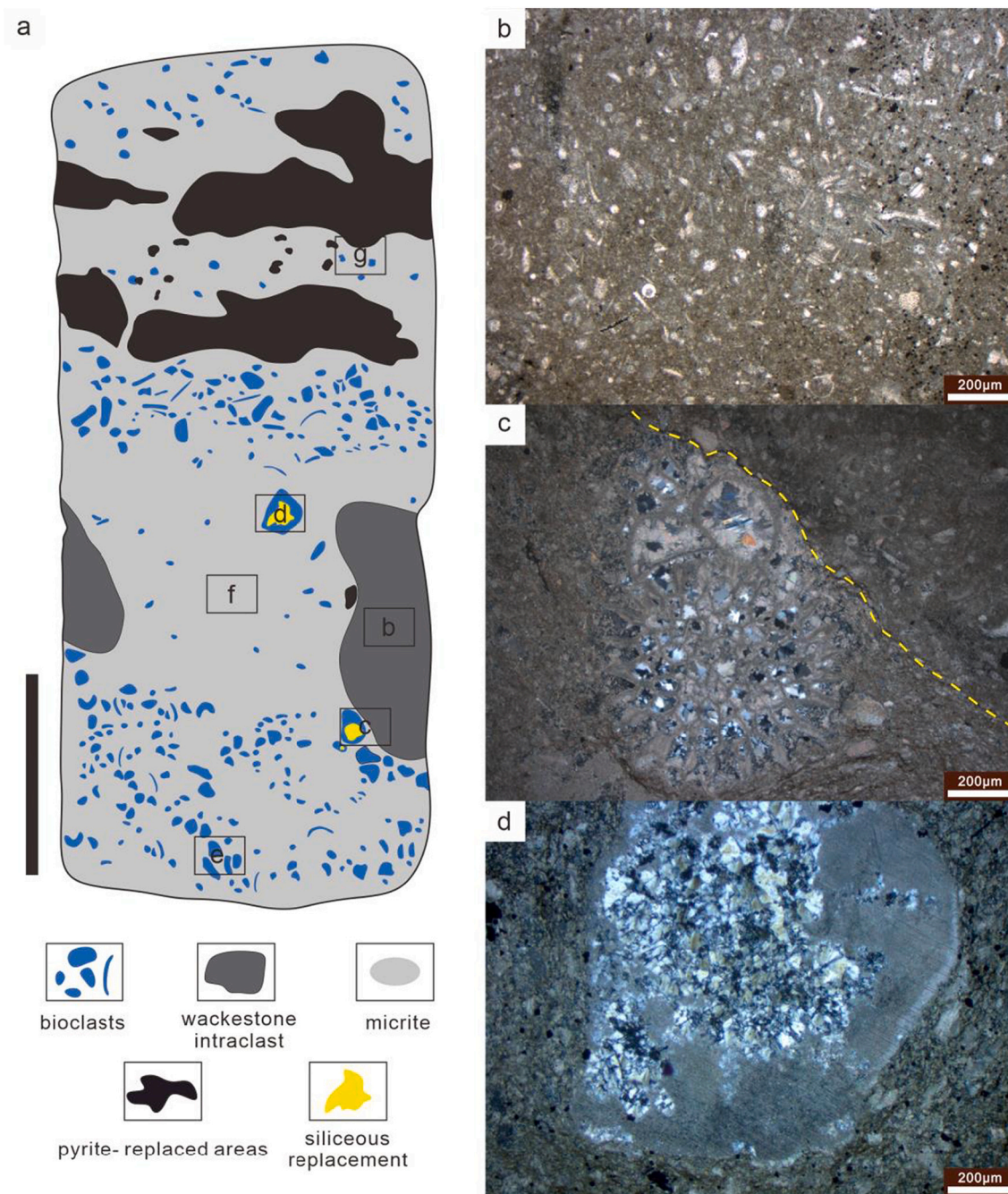


Fig. 4. Petrographic features of rudaceous limestone (sample JC-3). (a) sketch of lithofacies in limestone sample JC-3, consisting of bioclastic wackestone with intraclasts and abundant pyrite in the upper part. Black bar on the left side indicates a scale of 1 cm; positions of parts b, c and d are marked, and e, f and g refer to Fig. 3 parts c, b and d, respectively; (b) wackestone fabric within intraclast with small bioclast fragments; (c) bryozoan chambers infilled with quartz (cross polarized light). Dotted yellow line delineates the boundary of a wackestone intraclast; (d) large crinoid fragment with extensive siliceous replacement (cross polarized light). (For interpretation of the references to colour in this figure legend, the reader is referred to the web version of this article.)

and plot in the euxinic field (Fig. 9). The framboids from unit 4 are somewhat larger and more variable in size, and plot close to the euxinic/dysoxic boundary (Fig. 9). Framboids do not occur in the topmost sample (JC-21), although some pyrite crystals are present.

4.3. Geochemical proxies

4.3.1. TOC variability

TOC values in the Costigan carbonate are low, with an average of 0.09 ± 0.02 wt%, followed by a small increase in the phosphatic sandstone to 0.61 wt% (Table 1; Fig. 10). The onset of black shale in the

Exshaw Formation shows a sharp increase in TOC to 4.00 wt% and remains high, with average values of 4.12 ± 0.39 wt% throughout units 2 and 3. TOC levels in unit 4 decline to a value of 0.22 wt% at the top of succession (Table 1; Fig. 10).

4.3.2. Total Fe, total P and Fe speciation

Samples from the Costigan Member have a low total iron (Fe_T) content (< 0.5 wt%), with the exception of the sample from the topmost bed, where Fe_T is 6.80 wt% (Table 1, Fig. 10). These typically low carbonate Fe_T values are below the threshold generally considered to provide reliable Fe speciation and Fe/Al data for palaeoredox analysis

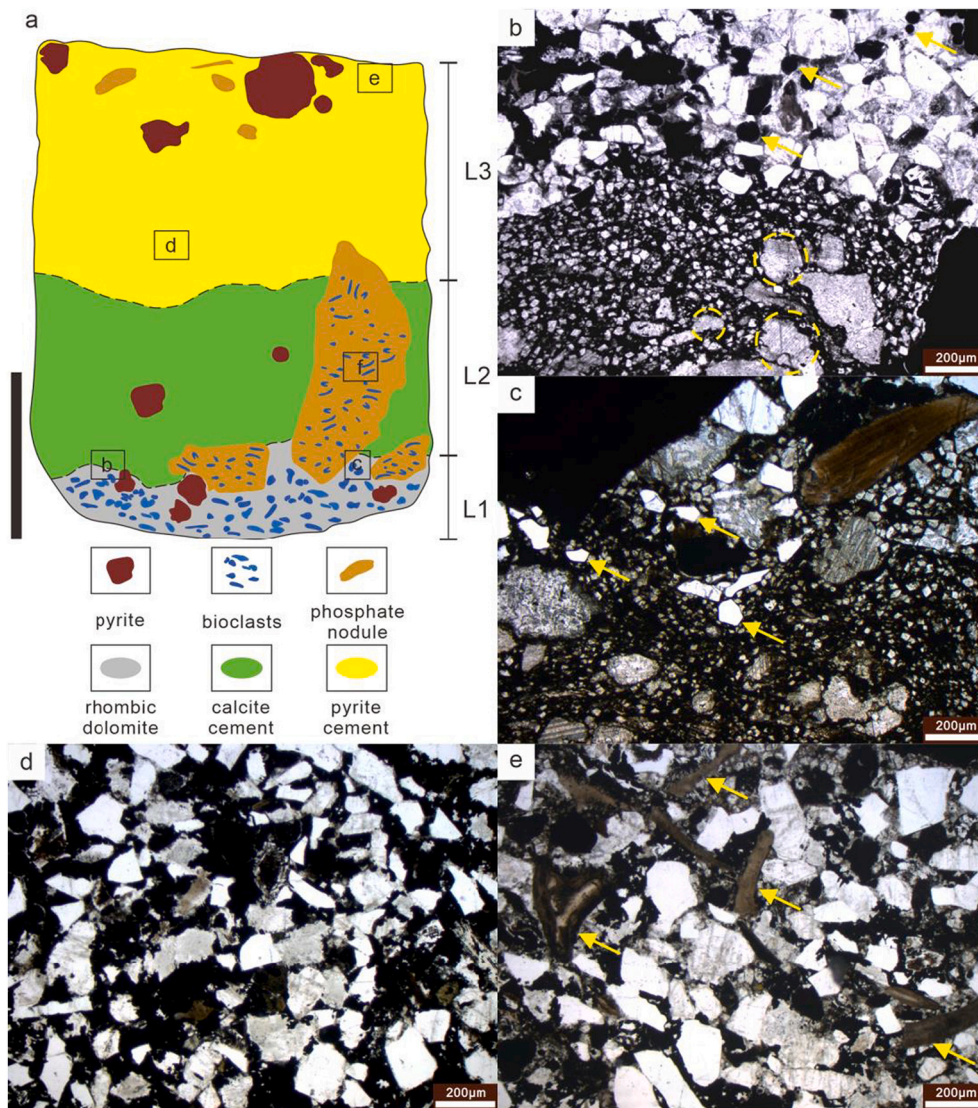


Fig. 5. Petrographic features of sample JC-4 (facies 2). (a) sketch of the lithofacies in the sandstone, showing three distinct layers. The black bar indicates a scale of 1 cm; positions of b, c and d are marked; f is the position of the SEM image in Fig. 6f. Photomicrographs showing: (b) rhombic dolomite and reworked crinoid fragments (some examples circled in yellow), and pyrite grains (yellow arrows) seen at contact between layers 1 and 2; (c) quartz grains (yellow arrows) with bioclasts and rhombic dolomite; (d) sand grains of quartz and feldspar cemented by pyrite in layer 3; (e) phosphatic bioclasts (yellow arrows), likely fish bones, in sandstone of layer 3. (For interpretation of the references to colour in this figure legend, the reader is referred to the web version of this article.)

(Clarkson et al., 2014), and thus are not considered further in this context. The Fe_T content increases dramatically in the phosphatic sandstone bed (to 9.22 wt%), and the black shales of unit 2 have an average of 2.25 ± 0.82 wt%. This is followed by lower values in the radiolarian-rich shale of unit 3, ranging from 0.21–1.36 wt%, and there is another sample (JC-11), containing low Fe_T , which will not be considered in Fe associated redox analysis (Table 1, Fig. 10). Concentrations of Fe_T increase again in the shales of unit 4, reaching 3.68 wt% before decreasing to 1.96 wt%.

The stratigraphic trend in Fe_T/Al , which may provide insight into variability in water column redox conditions (Lyons and Severmann, 2006; Clarkson et al., 2014), closely follows the trend seen in Fe_T through the Exshaw Shale, with a decline at the top of unit 2, stable and low values in unit 3, and an increase in unit 4 (Fig. 10). Variations in the proportions of Fe_{ox}/Fe_{HR} and Fe_{py}/Fe_{HR} show inverse trends, whereby Fe_{py} is high in the second and fourth interval, but low in the third, and Fe_{ox} is the main Fe_{HR} fraction in the third unit (Fig. 10; Table 1). The concentration of Fe_{carb} is also particularly low in unit 3, while Fe_{mag} is consistently low in all samples, averaging only 0.017 ± 0.006 wt% (Table 1). Fe_{HR}/Fe_T ratios are elevated (> 0.38), representing the threshold for distinguishing deposition beneath anoxic bottom waters (Raiswell and Canfield, 1998; Raiswell et al., 2001; Poulton and Raiswell, 2002) throughout the section, but with a slight decrease in unit 3

(Fig. 10).

Total phosphorus displays a similar trend to total Fe (Fig. 10). In detail, P is low throughout most of unit 1 (212 ± 32 ppm), but there is an increase to 1080 ppm in the topmost limestone sample, with a subsequent major increase to 12,090 ppm in the phosphatic sandstone (Table 1). Total P then returns to lower values of 313 ± 150 ppm in the black shale of unit 2, followed by particularly low average values of 131 ± 85 ppm in unit 3, and then an increase to 475 ± 42 ppm in unit 4.

4.3.3. Trace metals (Mo, U, V and Re)

Redox sensitive trace metal concentrations are low in carbonates of the Costigan Member, but Mo, U, V and Re all increase slightly towards the top (Fig. 11; Table 1). There are then large increases in Mo (to ~ 200 ppm), U (to ~ 32 ppm) and Re (to ~ 1065 ppb), and a smaller increase in V (to ~ 16 ppm), in the phosphatic sandstone of unit 2. The overlying calcareous black shale of unit 2 is characterized by overall high values of Mo (87.7 ± 32.8 ppm), U (21.5 ± 6.2 ppm) and Re (75.1 ± 58.4 ppb), but with significant scatter, while V progressively increases to reach a peak of ~ 1855 ppm around the level where large carbonate concretions occur (Fig. 11). Trace metal concentrations decline to relatively stable values in unit 3 (Mo = 65.5 ± 12.6 ppm; U = 10.0 ± 1.9 ppm; V = 1274 ± 161 ppm; Re = 48.7 ± 18.1 ppb). Unit 4 is characterized by markedly lower trace metal concentrations, although values tend to be higher than

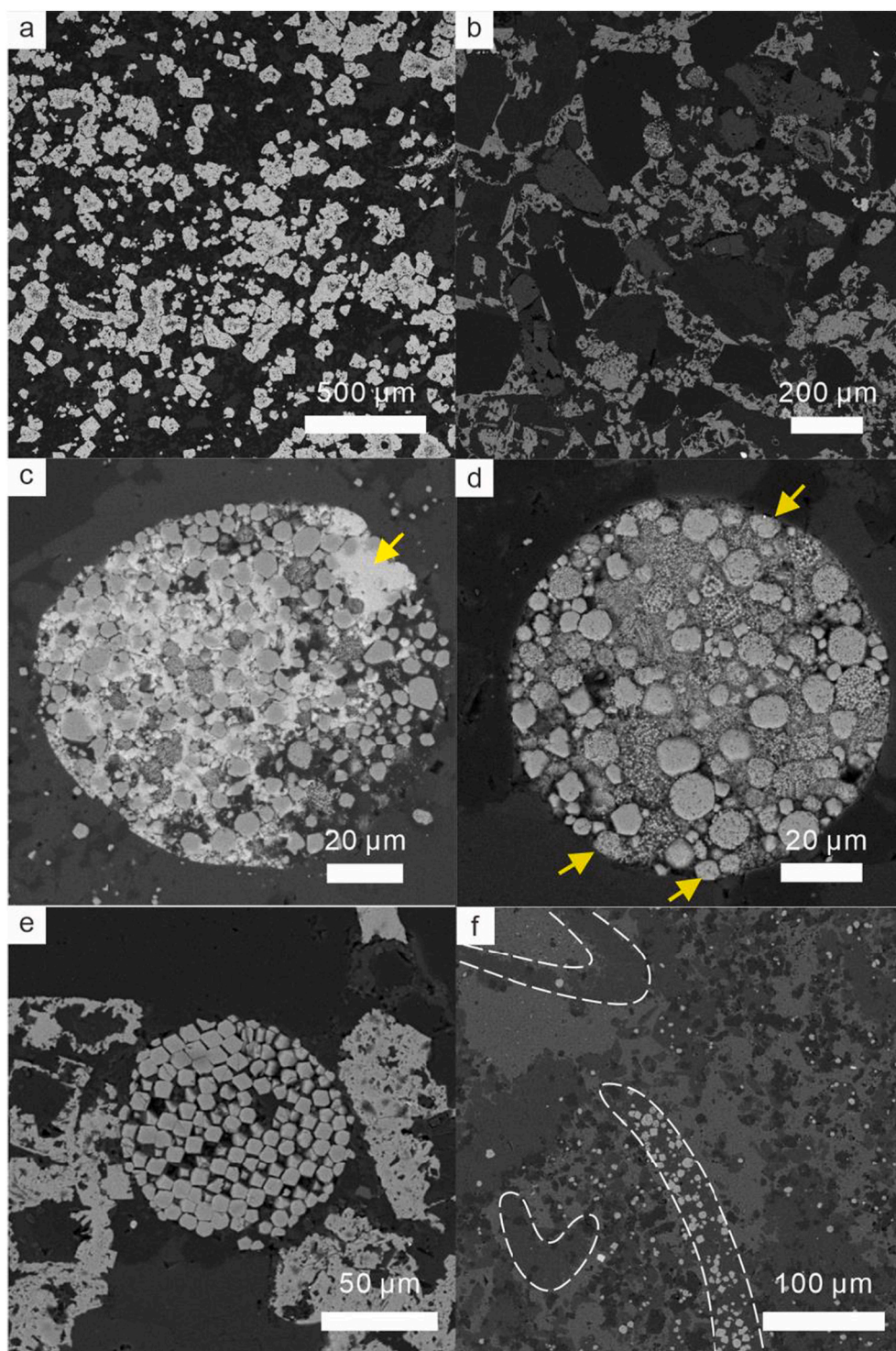


Fig. 6. SEM backscatter images of pyrite morphologies in limestone (sample JC-3) and sandstone (sample JC-4). (a) abundant pyrite crystals in sample JC-3; (b) pyrite cement between clastic grains (mainly quartz and feldspar) in sample JC-4; (c) polyframboid composed of framboids with pyrite microcrysts dominating the matrix in sample JC-4 (yellow arrows indicate truncated framboids at the margin); (d) polyframboid comprising framboids and pyrite crystals with a mostly cemented matrix of sphalerite (the brightest mineral, yellow arrow); (e) giant framboid composed of giant microcrysts of octahedral pyrite; (f) phosphate clasts in Fig. 5a consisting of bioclasts (dark area), partly replaced by pyrite crystals, and framboids (bright crystals circled by white dotted line). The matrix is phosphate-rich (medium grey area). (For interpretation of the references to colour in this figure legend, the reader is referred to the web version of this article.)

in the carbonates of unit 1 (Fig. 11; Table 1).

Enrichment factors for Mo, U, V and Re tend to closely follow the trends in the concentration data, although enrichment factors for Mo, U and V show a slight overall decrease through unit 3, which contrasts with concentration data for these elements (Fig. 11). Enrichment factors for all of the trace metals are particularly elevated (> 1) through units 2 and 3, indicating enhanced drawdown and sequestration in the sediment. We also use Re/U and Re/Mo ratios to evaluate water column and porewater redox conditions (see below). Both parameters decrease through unit 1, but show strong peaks in the phosphatic sandstone of

unit 2 (Fig. 11). Values then remain relatively constant, but with a slight overall increase, through units 2, 3 and 4, followed by peaks in both Re/U and Re/Mo in the uppermost sample of unit 4.

5. Discussion

5.1. Depositional conditions

5.1.1. Unit 1

The top 2 m of the Costigan Member at Jura Creek is a crinoidal

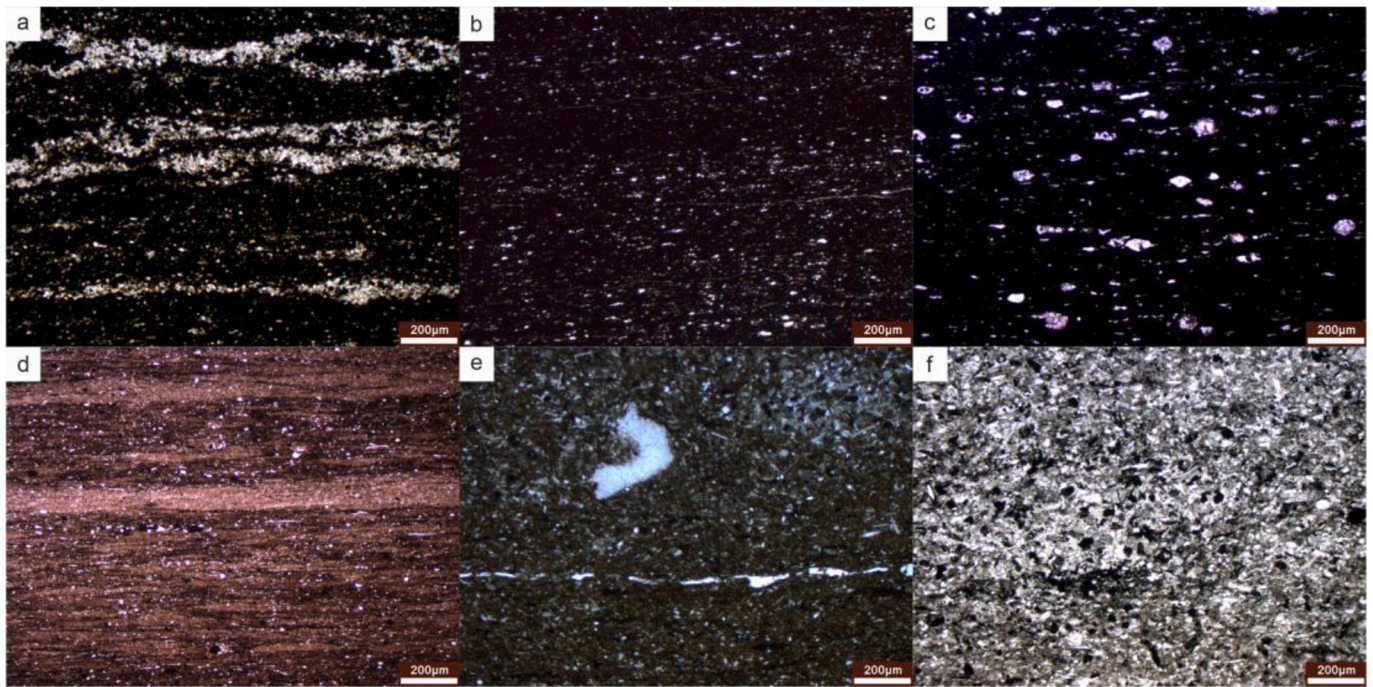


Fig. 7. Petrographic features of shale samples from the Black Shale Member at Jura Creek. (a) sample JC-5: calcareous black shale consisting of organic-rich layers and calcite-rich laminations, facies 3; (b) sample JC-6: siliceous black shale bearing tiny, scattered quartz grains, facies 4; (c) sample JC-12: siliceous black shale bearing abundant radiolarians, facies 4; (d) sample JC-20: lenticular laminated shale consisting of compacted clay clasts and silt, facies 5; (e) sample JC-19: calcareous mudstone bearing ophiuroid and tiny carbonate bioclasts, facies 6; (f) sample JC-21: pyritic calcareous silt, facies 7.

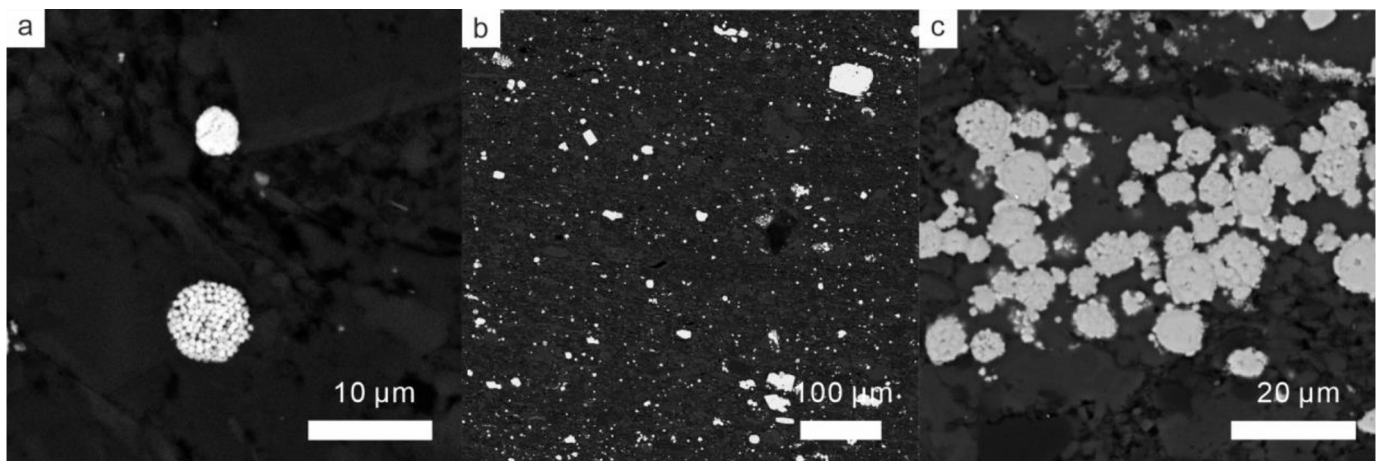


Fig. 8. SEM backscatter images of pyrite morphologies. (a) Sample JC-5: small framboids in calcareous black shale; (b) Sample JC-20 showing abundant pyrite crystals; (c) Sample JC-19: abundant framboids showing secondary pyrite overgrowth.

wackestone to packstone developed in a mid-ramp setting (Richards and Higgins, 1988; Savoy, 1992). The limestone contains low concentrations of Mo, U and V (Fig. 11), suggesting well-oxygenated bottom waters. In support of this contention, relatively high Re/U and Re/Mo ratios through most of the unit suggest that dysoxic conditions were likely limited to pore waters close to the sediment-water interface (Fig. 12a). However, during deposition of this unit, a progressive decrease in Re/U and an overall decrease in Re/Mo are accompanied by slight increases in the concentrations of U and Re in the uppermost sample (Fig. 10). These trends suggest that the redox state of the system was beginning to change, leading to the development of anoxic pore waters closer to the sediment-water interface during the final stages of unit 1 deposition (Fig. 12a). However, the lack of any significant increase in [V] in the uppermost sample (Fig. 10) suggests that the pore waters remained

dysoxic at the sediment-water interface. This relatively minor redox progression in the sediment, with strong evidence for oxic water column conditions, is in accord with the abundant and diverse benthic fauna seen in this unit (Figs. 3, 12a).

At the top of unit 1, the occurrence of reworked limestone pebbles (Fig. 2) suggests partial seafloor lithification and reworking, perhaps as accommodation space declined. Indeed, a depositional hiatus is reported between the top of the Costigan Member of the Palliser Formation and the base of the Exshaw Formation in the region (Savoy et al., 1999; Johnston et al., 2010), raising the possibility that carbonate production in the region was terminated by emergence (Smith et al., 1995). However, such a scenario appears unlikely given the ramp geometry during deposition of the Palliser Formation (Savoy, 1992), because a base-level fall would be unlikely to shut down deposition in the lower reaches of

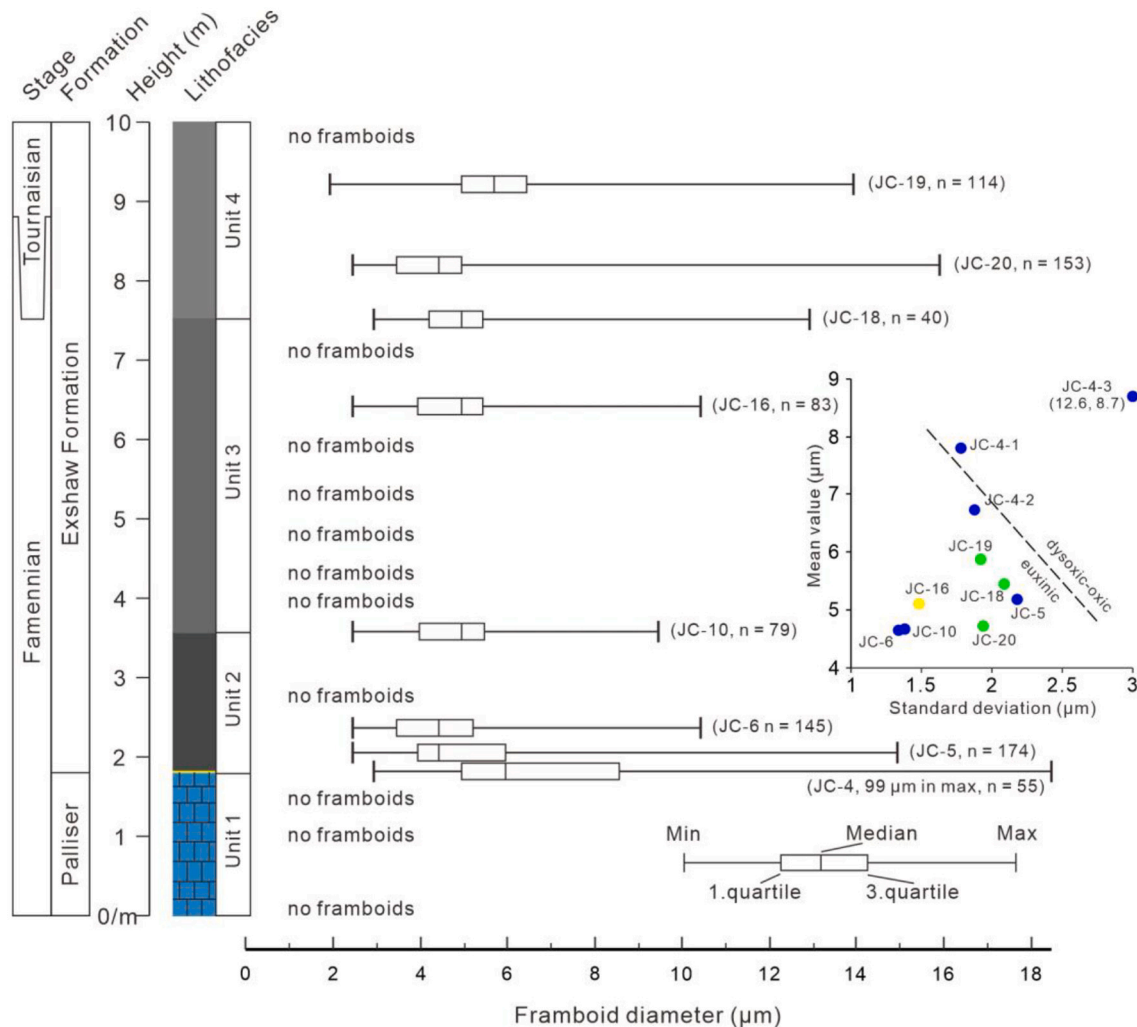


Fig. 9. Box-and-whisker plots of framboid size distributions from Jura Creek samples and mean value versus standard deviation plot. Blue, yellow and green circles represent statistic features of framboids in the second, third and fourth units, respectively. Data for samples JC-4-1 and JC-4-2 were collected from framboids within two polyframboids, while the framboid size distribution in sample JC-4-3 was collected from the sandstone matrix. (For interpretation of the references to colour in this figure legend, the reader is referred to the web version of this article.)

(they do not exceed 0.1 mm diameter), do not show half-filled examples, and lack the organic coating of the Schieber and Baird examples (although such material could have been removed by abrasion). Nonetheless, a *Tasmanites*-fill model for the Jura Creek polyframboids cannot be ruled out. Whatever their origin, it is clear that they have been subject to erosion and abrasion (Fig. 7c).

The process of erosion and polyframboid formation likely occurred in anoxic waters otherwise sulphide oxidation would have occurred. Similar examples of phosphate-and-pyrite-rich lag deposits, with polyframboids (and *Tasmanites* infills), are seen at the base of black shale successions from the Devonian of eastern USA, for which Baird and Brett (1991) developed an internal wave-erosion model. Such waves develop at the density interface in stratified basins, and can separate an anoxic lower water column from a better mixed upper water column. Wave erosion combined with carbonate dissolution is envisaged to be intense, resulting in a remnant lag of phosphate and pyrite grains (Baird and Brett, 1991).

The Jura Creek bed only differs from the examples described by Baird and Brett (1991) in its siliciclastic component, which is envisaged to derive from a western, volcanic source (Savoy, 1992). The angularity of the grains suggests their transport distances were short (Fig. 5). The phosphatic sandstone also contains substantial amounts of biogenic phosphate (fish bones) that are likely to have accumulated slowly from a

pelagic rain (Fig. 12c). During this stage a series of diagenetic phases formed within the sandstone, comprising dolomite rhombs (Fig. 5b), calcite and pyrite cement (Fig. 7b), and sphalerite cement within some polyframboids (Fig. 7d).

The subsequent onset of calcareous black shale deposition records a quiescent depositional environment, with occasional currents introducing calcisilt laminae as bed load or dense suspension (Fig. 6a). The calcisilt was derived from up-dip, implying that the carbonate factory was weakly re-established in shallower settings at this time (Fig. 12d). Thus, the phosphatic sandstone records the onset of water column deoxygenation, whilst the overlying siliceous black shales of unit 2 formed as these conditions intensified. A sharp increase in TOC at the base of the black shale coincides with elevated Fe/Al, Fe_{HR}/Fe_T and Fe_{py}/Fe_{HR} (Fig. 10), as well as enrichments in Mo and U (Fig. 11). In combination with the small size and narrow range of pyrite framboids in this interval (Fig. 9, Table 3), these observations provide strong support for a transition to euxinic water column conditions (Fig. 12d). Given this redox reconstruction, the low V_{EF} values at this horizon likely reflect the lack of a Mn shuttle under euxinic conditions, which, as observed in some modern euxinic environments, would limit transport of V to the sediment (Bennett and Canfield, 2020).

There is a progressive decrease in Mo_{EF} , U_{EF} and Re_{EF} (Fig. 11) towards the middle part of unit 2 (samples JC-5 to JC-7), and pyrite

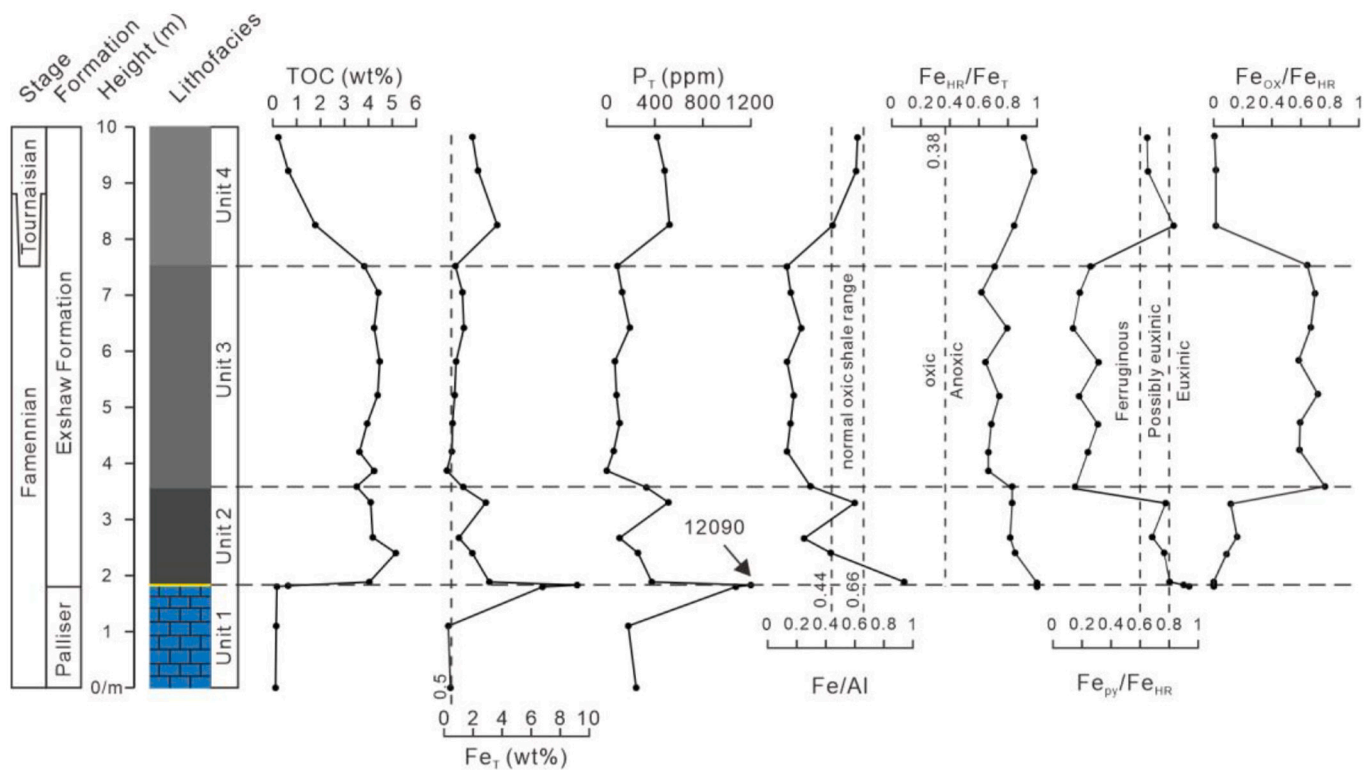


Fig. 10. Geochemical profiles for total Fe (Fe_T), total P (P_T) and Fe speciation through the Jura Creek section. The dashed line on Fe_T plots represent the minimum Fe concentration (0.5 wt%) for application of Fe speciation. The dashed lines on Fe/Al plots represent the range of normal oxic shale (0.44–0.66) (Clarkson et al., 2014). The dashed line on Fe_{HR}/Fe_T plots represent the boundary for distinguishing anoxic water-column conditions. The dashed lines on Fe_{Py}/Fe_{HR} plots represent the boundaries for distinguishing euxinic (> 0.8) and ferruginous (< 0.6) water-column conditions.

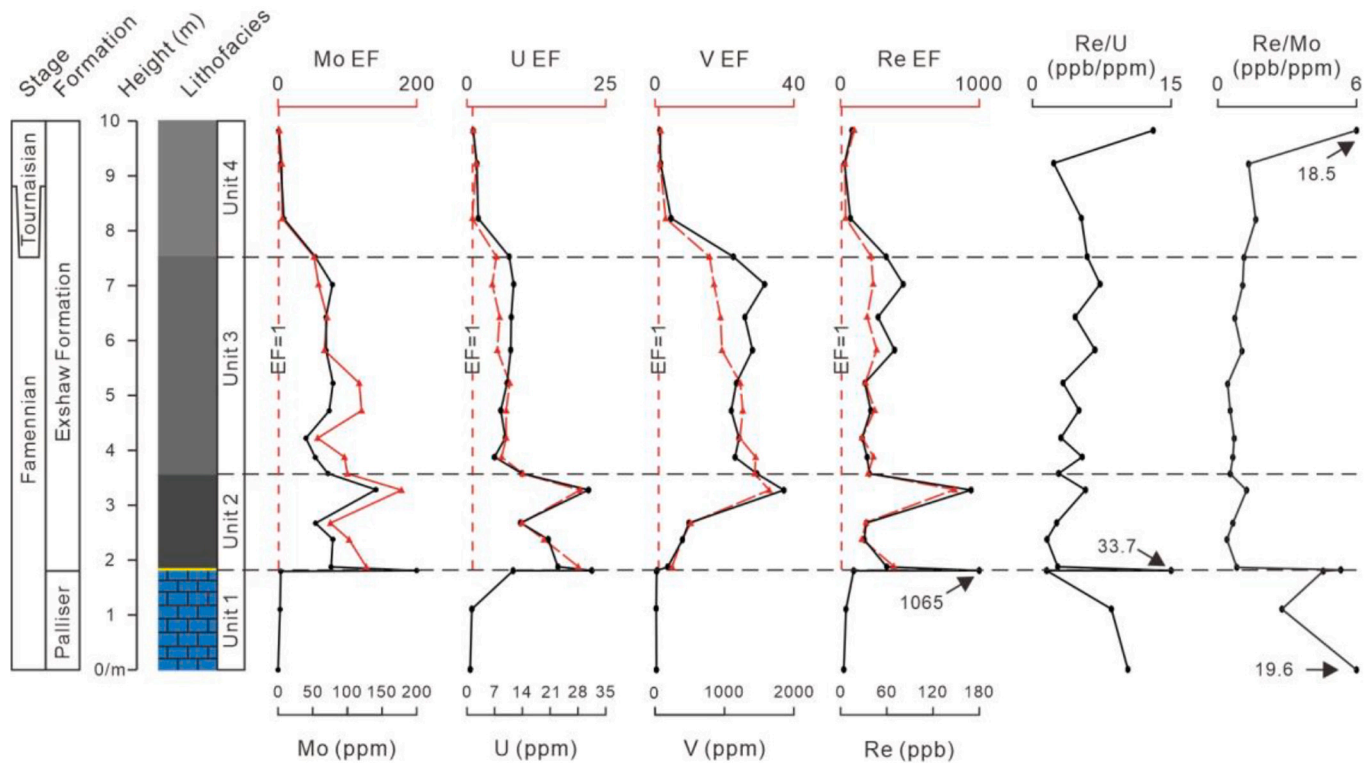


Fig. 11. Redox sensitive element profiles for the Jura Creek section. Black solid lines represent concentrations, and red lines with triangle icons represent variation in enrichment factors. (For interpretation of the references to colour in this figure legend, the reader is referred to the web version of this article.)

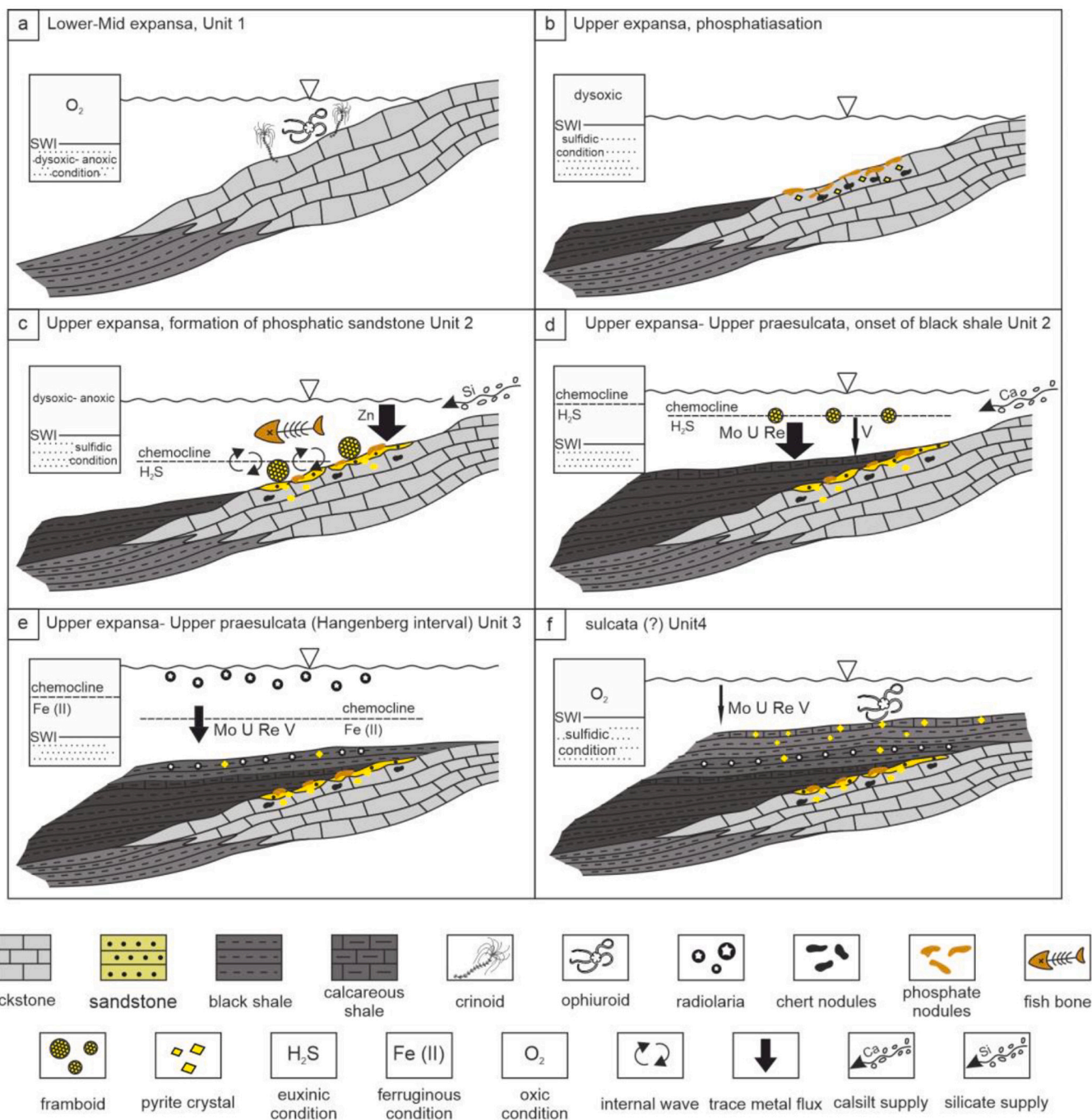


Fig. 12. Redox evolution and depositional history of the Devonian-Carboniferous transition in western Canada. Inset boxes show redox conditions at the Jura Creek study site (location indicated by triangle in main figures). The size of arrows is consistent with the amount of trace metal flux. SWI is sediment- water interface.

framboids are absent in samples of JC-7 (Fig. 9). By contrast, Fe_{HR}/Fe_T and Fe_{py}/Fe_{HR} ratios remain elevated (Fig. 10), while V_{EF} values increase through this part of the succession (Fig. 10). This implies that water column redox conditions fluctuated through unit 2, with an overall progression to less intense euxinia, and likely ferruginous conditions (but with the development of sulphidic porewaters during diagenesis resulting in elevated Fe_{py}/Fe_{HR}), towards the middle of the unit. In this context, the low Fe_T/Al ratios in the middle of unit 2, which are substantially depleted relative to average shale (Fig. 10), may partly represent intense recycling of Fe_{HR} between the sediments and water column, whereby short-term delivery of Fe_{HR} to the sediment by water column precipitation under ferruginous conditions was followed by Fe recycling during diagenesis and Fe^{2+} supply back to the water column

(Poulton and Canfield, 2011; Poulton, 2021). Such a scenario, likely requiring variable redox conditions on short timescales (which would be integrated over the timescale recorded by our sampling strategy), could potentially account for the complex redox signal recorded at this horizon, but does imply that the Fe_T/Al ratio of the detrital sediment supplied to this region was low relative to average shale.

The upper half of unit 2 then records the re-establishment of more intense euxinia (as indicated by elevated MO_{EF} , U_{EF} , V_{EF} and Re_{EF} values; Fig. 10), prior to the boundary with unit 3. This overall evolution of redox conditions is supported by the co-behaviour of MO_{EF} and U_{EF} (Fig. 13), whereby the samples through the lower half of unit 2 (samples JC-5 to JC-7) transition from the euxinic field to the particulate shuttle field, with a return to the euxinic field in the upper half of unit 2 (sample

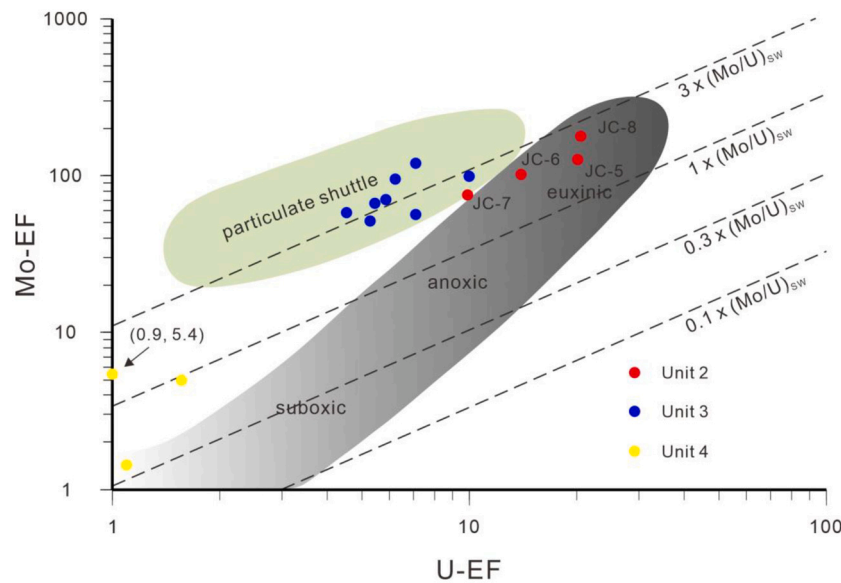


Fig. 13. Mo-EF versus U-EF cross plot for the Jura Creek section. Unit 2 samples are labelled to show the progression of redox conditions through this unit. Cross plot is modified from Algeo and Tribovillard (2009) and Tribovillard et al. (2012).

JC-8), before a return to the particulate shuttle field at the boundary between units 2 and 3 (Fig. 13).

5.1.3. Unit 3

Radiolarians are typically oceanic taxa although they can also occur in coastal regions (e.g. Lampitt et al., 2009). The appearance of radiolarians in unit 3, at a level within the *praesulcata* Zone (and thus equivalent to the Hangenberg Event in Europe (Richards and Higgins, 1988)), suggests improved oceanic connectivity, probably associated with continued deepening (Fig. 12e). Unit 3 is characterized by high Fe_{HR}/Fe_T and low Fe_{py}/Fe_{HR} ratios (Fig. 10) and an absence of pyrite framboids, suggesting anoxic, ferruginous, water column conditions. This redox state is supported by the moderate Mo_{EF} , U_{EF} , V_{EF} and Re_{EF} values (Fig. 11), and in particular, the Mo_{EF} and U_{EF} data that plot in the particulate shuttle region (Algeo and Tribovillard, 2009), suggesting elevated Mo drawdown through uptake by Fe minerals precipitating in a ferruginous water column (Fig. 13).

As with the development of ferruginous conditions in the middle part of unit 2, ferruginous condition in unit 3 are associated with very low Fe_T/Al ratios (Fig. 10). As discussed above, the Fe_T/Al ratio of detrital sediment delivered to this region may have been particularly low relative to average shale, thus partially explaining the lack of enrichment in Fe_T . However, we also note that low Fe_T/Al ratios often occur in deep-water siliceous sediments deposited under ferruginous conditions and could potentially be generated through diagenesis. During diagenesis of biogenic silica in sediment, dissolution of detrital minerals (clay minerals) releases dissolved Al to pore waters, which then becomes structurally incorporated into the deposited biogenic silica (Van Cappellen and Qiu, 1997; Dixit et al., 2001; Van Cappellen et al., 2002). The dissolution of detrital minerals would also release dissolved Fe^{2+} , which would be retained in the sediment as Fe_{HR} under oxic conditions. However, in contrast to Al, under ferruginous conditions the mobilised Fe would have the potential to diffuse into the water column (Poulton and Canfield, 2011; Poulton, 2021), particularly in non-sulphidic sediments where precipitation of pyrite would not act as a sink for the Fe^{2+} . This scenario would be expected in the radiolarian-rich sediments of unit 3, whereby an Fe_{HR} mineral shuttle sequestered Mo in the sediment, but recycling back to the water column of a portion of this Fe_{HR} under non-sulphidic conditions close to the sediment-water interface, along with the Fe^{2+} released through detrital mineral dissolution, would result in the distinct combination of elevated Fe_{HR}/Fe_T ratios and low Fe_T/Al

ratios. Indeed, we note that generation of this combined Fe signal may be a distinctive and possibly even a diagnostic feature of biogenic silica-rich sediments deposited under ferruginous conditions.

5.1.4. Unit 4

The appearance of bioclasts in the calcareous mudstone indicates improved benthic oxygenation of the sea floor during deposition of unit 4 at the start of the Carboniferous. A decline in Mo_{EF} , U_{EF} , V_{EF} and Re_{EF} (Fig. 11), combined with the Mo_{EF} - U_{EF} cross-plot systematics (Fig. 13), all support progressive oxygenation. Increases of Re/U and Re/Mo in the topmost sample suggest a transition from anoxic to dysoxic pore waters close to the sediment-water interface, thus providing further evidence for a progressive return to a well-oxygenated marine environment (Fig. 12f). However, Fe_{HR}/Fe_T and Fe_{py}/Fe_{HR} are high (and Fe_T/Al also increases) in this unit, with SEM observations suggesting that the pyrite comprises euhedral crystals and is therefore diagenetic in origin (Fig. 8). Consequently, the high Fe_{py}/Fe_{HR} ratio reflects intense sulphide production deeper in the pore waters (Poulton, 2021), with the elevated Fe_{HR}/Fe_T and Fe_T/Al ratios likely arising from water column precipitation of Fe minerals during upwelling of deeper ferruginous waters into the shallower dysoxic waters.

5.2. Models for carbonate shutdown

Carbonate demise in the western Laurentia during the Famennian has been attributed to the role of increased nutrient supply from upwelling, with the increased productivity and declining seafloor oxygenation being responsible for carbonate shutdown (e.g. Savoy, 1992; Caplan et al., 1996; Caplan and Bustin, 1999). Here we show evidence of increasing dysoxia in the uppermost levels of the Costigan Member and the associated phosphogenesis provides substantial support for this scenario. However, the reliance on upwelling to elevate nutrient levels is questionable. The Devonian-Carboniferous transition along the western North American margin coincides with the Antler Orogeny and the development of a foreland basin (Root, 2001); such a transition would likely have restricted the regions connectivity with the global ocean and its nutrients. Potentially any decline in connection may have been overridden by an increase in oceanic circulation. Global cooling and glaciation in the latest Famennian are frequently argued to have invigorated upwelling and so lead to the development of Hangenberg anoxia (Caplan and Bustin, 1999; Bábek et al., 2016; Kumpan et al.,

2019). The best evidence for glaciation occurs in the mid-*praesulcata* Zone where sea-level fall lead to incision and valley fill (e.g. the Hangenberg Sandstone; Fig. 1), but these events postdate carbonate shutdown in Canada. Rather than upwelling, nutrients may have been derived from land; the occurrence of terrestrial grains in the phosphatic sandstone supports this possibility. It is interesting to note that, by the time of Hangenberg black shale development in Europe, the Jura Creek section showed peak water depths (radiolarian-rich black shale) which potentially could have had improved oceanic connectivity and access to upwelled nutrients. Instead, water column redox conditions changed from euxinic to ferruginous anoxic around this time, indicating slight improvement in oxygenation. Clearly, the redox conditions in western Laurentia were not entirely driven by variations in nutrient supply. The semi-isolation of the deep-water basins was likely a key factor (e.g. Caplan and Bustin, 2001; Algeo et al., 2007).

5.3. Comparative latest Devonian redox history in other North American basins

The redox history of other basins in North America during the Devonian-Carboniferous transition bears some comparison with the Western Canada Sedimentary Basin albeit with regional differences. The Lower Bakken Formation of the Williston Basin is both organic-carbon rich (total organic carbon values average 9.7 wt%) and trace metal rich suggesting euxinic deposition possibly with sulphidic conditions developed within the photic zone (Scott et al., 2017). This is broadly comparable with the euxinic-style deposition proposed for the contemporaneous black shales of unit 2 at the base of the Exshaw Formation at Jura Creek. In contrast, the Middle Member of the Bakken Formation, a succession of mixed carbonate-siliciclastic beds (roughly coeval with units 3 and 4 at Jura Creek), records substantially better ventilation than seen in the Western Canada Sedimentary Basin likely due to a shallower depositional setting (Egenhoff, 2017; Hogancamp and Pocknall, 2018; Hart and Hofmann, 2018). The Sappington Basin also saw intense euxinic deposition during deposition of the Lower Sappington Formation in the Mid *expansa* Zone (di Pasquo et al., 2019; Browne et al., 2020), and again this of broadly comparable age to unit 2 at Jura Creek. Following a hiatus in the Sappington Basin, the resumption of deposition in the Upper *expansa* Zone saw better oxygenated carbonates and siliciclastics developed in a basin interpreted to be brackish rather than fully marine (Browne et al., 2020).

What the basins of western North America do not show is an intensification of anoxia comparable to that seen during the Hangenberg crisis in Europe. It seems likely that this signal was substantially overprinted by regional controls on basin development, that are no doubt linked to the ongoing Antler orogeny. In most sections the most anoxic conditions are developed earlier, during the *expansa* Zone, whilst the Hangenberg Crisis, in the *praesulcata* interval saw the transition from euxinic to ferruginous conditions in our Western Canada Sedimentary Basin study and an even greater improvement of oxygenation in the Sappington and Williston Basins.

6. Conclusions

The trigger of anoxia and its impact on the carbonate ramp in western Laurentia during the latest Famennian has been subject to considerable debate. Evidence from the Jura Creek type section of the Exshaw Formation shows that the final stages of limestone deposition in the Costigan Member of the Palliser Formation were likely caused by declining oxygen levels (shown by decreasing Re/U and Re/Mo levels) and associated phosphogenesis. This suggests eutrophication with increased nutrient flux driving the change. It is unlikely the nutrients were sourced from oceanic upwelling, given the restricted connections to the global ocean due to the existence of a physical barrier to the west. Following the shutdown of carbonate productivity, the subsequent passage of a dissolutional pycnocline caused deflation of the top surface

of the limestone and the formation of a thin lag of phosphate and pyrite clasts in a sandstone. The latter include extraordinarily large framboids and polyframboids that accreted in agitated, anoxic bottom waters.

The redox history of the Black Shale Member shows considerable variations. Euxinic conditions became established during deposition of the lowest part of the Shale as indicated by enriched U and Mo values, elevated Fe/Al, Fe_{HR}/Fe_T and Fe_{py}/Fe_{HR} and the presence of populations of small framboids. Only V is not enriched, which may reflect the lack of a Mn shuttle in the sulfidic water column. The middle part of the Black Shale Member is contemporaneous with the Hangenberg black shale event in Europe and, unusually for a black shale, it lacks any pyrite framboids. This petrographic observation is supported by the very low Fe_{py}/Fe_{HR} values at this level, although Fe_{HR}/Fe_T are high and Fe_T/Al low. These are the attributes of ferruginous anoxic conditions in which much remobilised Fe escapes to the water column. Redox history from other basins in western North America (the Sappington and Williston basins) show even greater improvements in basin ventilation. The Hangenberg anoxic event is barely manifest in the region. The younger, Carboniferous levels of the Black Shale Member record a transition to dysoxic conditions. Despite the diverse history of redox change recorded in this study, the organic carbon values of the Black Shale Member at Jura Creek remained remarkably constant at values of ~4 wt% TOC, before declining in the uppermost dysoxic level.

Declaration of Competing Interest

I am Sen Li, on behalf of all coauthor, declare that our manuscript have no known competing financial interests or personal relationships that could have appeared to influence the work reported in this paper.

Acknowledgements

Dr. Yijun Xiong and Dr. Tianchen He are acknowledged for their support in geochemical analysis. Our gratitude also extends to Lisa Neville who helped with field work and sample collection. We thank an anonymous reviewer and Song Huyue for their comments during the review process.

References

- Alcott, L.J., Krause, A.J., Hammarlund, E.U., Bjerrum, C.J., Scholz, F., Xiong, Y., Hobson, A.J., Neve, L., Mills, B.J.W., März, C., Schnetger, B., Bekker, A., Poulton, S.W., 2020. Development of iron speciation reference materials for Palaeoredox analysis. *Geostand. Geoanal. Res.* 44, 581–591. <https://doi.org/10.1111/ggr.12342>.
- Algeo, T.J., Tribovillard, N., 2009. Environmental analysis of paleoceanographic systems based on molybdenum-uranium covariation. *Chem. Geol.* 268, 211–225. <https://doi.org/10.1016/j.chemgeo.2009.09.001>.
- Algeo, T.J., Lyons, T.W., Ronald, B., Over, D.J., 2007. Hydrographic conditions of the Devonian–Carboniferous North American Seaway inferred from sedimentary Mo–TOC relationships. *Palaeogeogr. Palaeoclimatol. Palaeoecol.* 256, 204–230. <https://doi.org/10.1016/j.palaeo.2007.02.035>.
- Anderson, R.F., Lehuray, A.P., Fleisher, M.Q., Murray, J.W., 1989. Uranium deposition in Saanich Inlet sediments, Vancouver Island. *Geochim. Cosmochim. Acta* 53, 2205–2213. [https://doi.org/10.1016/0016-7037\(89\)90344-X](https://doi.org/10.1016/0016-7037(89)90344-X).
- Bábek, O., Kumpan, T., Kalvoda, J., Matys Grygar, T., 2016. Devonian/Carboniferous boundary glacioeustatic fluctuations in a platform-to-basin direction: A geochemical approach of sequence stratigraphy in pelagic settings. *Sediment. Geol.* 337, 81–99. <https://doi.org/10.1016/j.sedgeo.2016.03.009>.
- Baird, G.C., Brett, C.E., 1991. Submarine erosion on the anoxic sea floor: stratigraphic, palaeoenvironmental, and temporal significance of reworked pyrite and bone deposits. *Geol. Soc. London Spec. Publ.* 58, 233–257. <https://doi.org/10.1144/GSL.SP.1991.058.01.16>.
- Becker, R.T., 1993. Anoxia, eustatic changes, and Upper Devonian to Lowermost Carboniferous global ammonoid diversity. In: House, M.R. (Ed.), *The Ammonoidea, Environment, Ecology, and Evolutionary Change*. Syst. Assoc. Spec. 47. Clarendon Press, Oxford, pp. 115–164.
- Benkovitz, A., Matthews, A., Teutsch, N., Poulton, S.W., Bar-Matthews, M., Almagi-Labin, A., 2020. Tracing water column euxinia in eastern Mediterranean sapropels S5 and S7. *Chem. Geol.* 545, 119627. <https://doi.org/10.1016/j.chemgeo.2020.119627>.
- Bennett, W.W., Canfield, D.E., 2020. Redox-sensitive trace metals as paleoredox proxies: A review and analysis of data from modern sediments. *Earth-Sci. Rev.* 204, 103175. <https://doi.org/10.1016/j.earscirev.2020.103175>.

- Bertine, K.K., Turekian, K.K., 1973. Molybdenum in marine deposits. *Geochim. Cosmochim. Acta* 37, 1415–1434. [https://doi.org/10.1016/0016-7037\(73\)90080-X](https://doi.org/10.1016/0016-7037(73)90080-X).
- Borovsky, D., Egenhoff, S., Fishman, N., Maletz, J., Boehlke, A., Lowers, H., 2017. Sedimentology, facies architecture, and sequence stratigraphy of a Mississippian black mudstone—The upper member of the Bakken Formation, North Dakota, United States. *AAPG Bull.* 101, 1625–1673. <https://doi.org/10.1306/01111715183>.
- Browne, T.N., Hofmann, M.H., Malkowski, M.A., Wei, J., Sperling, E.A., 2020. Redox and paleoenvironmental conditions of the Devonian-Carboniferous Sappington formation, southwestern Montana, and comparison to the Bakken Formation, Williston Basin. *Palaeogeogr. Palaeoclimatol. Palaeoecol.* 560, 110025. <https://doi.org/10.1016/j.palaeo.2020.110025>.
- Canfield, D.E., Raiswell, R., Westrich, J.T., Reaves, C.M., Berner, R.A., 1986. The use of chromium reduction in the analysis of reduced inorganic sulfur in sediments and shales. *Chem. Geol.* 54, 149–155. [https://doi.org/10.1016/0009-2541\(86\)90078-1](https://doi.org/10.1016/0009-2541(86)90078-1).
- Caplan, M.L., Bustin, R.M., 1999. Devonian-Carboniferous Hangenberg mass extinction event, widespread organic-rich mudrock and anoxia: causes and consequences. *Palaeogeogr. Palaeoclimatol. Palaeoecol.* 148, 187–207. [https://doi.org/10.1016/S0031-0182\(98\)00218-1](https://doi.org/10.1016/S0031-0182(98)00218-1).
- Caplan, M.L., Bustin, R.M., 2001. Palaeoenvironmental and palaeoceanographic controls on black, laminated mudrock deposition: example from Devonian-Carboniferous strata, Alberta, Canada. *Sediment. Geol.* 145, 45–72. [https://doi.org/10.1016/S0037-0738\(01\)00116-6](https://doi.org/10.1016/S0037-0738(01)00116-6).
- Caplan, M.L., Bustin, R.M., Grimm, K.A., 1996. Demise of a Devonian-Carboniferous carbonate ramp by eutrophication. *Geology* 24, 715–718. [https://doi.org/10.1130/0091-7613\(1996\)024<0715:DOADCC>2.3.CO;2](https://doi.org/10.1130/0091-7613(1996)024<0715:DOADCC>2.3.CO;2).
- Carmichael, S.K., Waters, J.A., Batchelor, C.J., Coleman, D.M., Suttner, T.J., Kido, E., Moore, L.M., Chadimová, L., 2016. Climate instability and tipping points in the Late Devonian: detection of the Hangenberg Event in an open oceanic island arc in the Central Asian Orogenic Belt. *Gondwana Res.* 32, 213–231. <https://doi.org/10.1016/j.gr.2015.02.009>.
- Clarkson, M.O., Poulton, S.W., Guilbaud, R., Wood, R.A., 2014. Assessing the utility of Fe/Al and Fe-speciation to record water column redox conditions in carbonate-rich sediments. *Chem. Geol.* 382, 111–122. <https://doi.org/10.1016/j.chemgeo.2014.05.031>.
- Crusius, J., Calvert, S., Pedersen, T., Sage, D., 1996. Rhenium and molybdenum enrichments in sediments as indicators of oxic, suboxic and sulfidic conditions of deposition. *Earth Planet. Sci. Lett.* 145, 65–78. [https://doi.org/10.1016/S0012-821X\(96\)00204-X](https://doi.org/10.1016/S0012-821X(96)00204-X).
- di Pasquo, M., Grader, G.W., Kondas, M., Doughty, P.T., Filipiak, P., Rice, B.J., Isaacson, P.E., 2019. Lower Sappington formation palynofacies in Montana confirm upper famennian black shale paleoenvironments and sequences across western North America. *Palaeogeogr. Palaeoclimatol. Palaeoecol.* 536, 109370. <https://doi.org/10.1016/j.palaeo.2019.109370>.
- Dixit, S., Van Cappellen, P., Van Bennekom, A.J., 2001. Processes controlling solubility of biogenic silica and pore water build-up of silicic acid in marine sediments. *Mar. Chem.* 73, 333–352. [https://doi.org/10.1016/S0304-4203\(00\)00118-3](https://doi.org/10.1016/S0304-4203(00)00118-3).
- Egenhoff, S.O., 2017. The lost Devonian sequence – sequence stratigraphy of the middle Bakken member, and the importance of clastic dykes in the lower Bakken member shale, North Dakota, USA. *Mar. Pet. Geol.* 81, 278–293. <https://doi.org/10.1016/j.marpetgeo.2017.01.015>.
- Egenhoff, S.O., Fishman, N.S., 2013. Traces in the dark-sedimentary processes and facies gradients in the upper shale member of the Upper Devonian-Lower Mississippian Bakken Formation, Williston Basin, North Dakota, U.S.A. *J. Sediment. Res.* 83, 803–824. <https://doi.org/10.2110/jsr.2013.60>.
- Emerson, S.R., Huested, S.S., 1991. Ocean anoxia and the concentrations of molybdenum and vanadium in seawater. *Mar. Chem.* 34, 177–196. [https://doi.org/10.1016/0304-4203\(91\)90002-E](https://doi.org/10.1016/0304-4203(91)90002-E).
- Erickson, B.E., Helz, G.R., 2000. Molybdenum(VI) speciation in sulfidic waters. *Geochim. Cosmochim. Acta* 64, 1149–1158. [https://doi.org/10.1016/S0016-7037\(99\)00423-8](https://doi.org/10.1016/S0016-7037(99)00423-8).
- Föllmi, K.B., 1996. The phosphorus cycle, phosphogenesis and marine phosphate-rich deposits. *Earth-Sci. Rev.* 40, 55–124. [https://doi.org/10.1016/0012-8252\(95\)00049-6](https://doi.org/10.1016/0012-8252(95)00049-6).
- Föllmi, K.B., 2016. Sedimentary condensation. *Earth-Sci. Rev.* 152, 143–180. <https://doi.org/10.1016/j.earscirev.2015.11.016>.
- Föllmi, K.B., Weissert, H., Funk, H., 1994. Evolution Along the Lower Cretaceous Northern Tethyan Margin, pp. 729–746. [https://doi.org/10.1130/0016-7606\(1994\)106<0729:PCISAC>2.3.CO;2](https://doi.org/10.1130/0016-7606(1994)106<0729:PCISAC>2.3.CO;2).
- Hart, B., Hofmann, M., 2018. The Late Devonian ice age and the giant Bakken oil field. *Sediment. Rec.* 18, 4–9.
- Helz, G.R., Miller, C.V., Charnock, J.M., Mosselmans, J.F.W., Patrick, R.A.D., Garner, C. D., Vaughan, D.J., 1996. Mechanism of molybdenum removal from the sea and its concentration in black shales: EXAFS evidence. *Geochim. Cosmochim. Acta* 60, 3631–3642. [https://doi.org/10.1016/0016-7037\(96\)00195-0](https://doi.org/10.1016/0016-7037(96)00195-0).
- Hogancamp, N.J., Pocknall, D.T., 2018. The biostratigraphy of the Bakken Formation: a review and new data. *Stratigraphy* 15, 197–224.
- Hornung, T., Brandner, R., Krystyn, L., Joachimski, M.M., Keim, L., 2007. Multistratigraphic constraints on the NW Tethyan “Carnian Crisis”. In: Lucas, S.G., Spielmann, J.A. (Eds.), *The Global Triassic*, 41. *New Mexico Mus. Nat. Hist. Sci Bull.*, pp. 59–67.
- Ingall, E.D., Van Cappellen, P., 1990. Relation between sedimentation rate and burial of organic phosphorus and organic carbon in marine sediments. *Geochim. Cosmochim. Acta* 54, 373–386. [https://doi.org/10.1016/0016-7037\(90\)90326-G](https://doi.org/10.1016/0016-7037(90)90326-G).
- Johnston, D.I., Henderson, C.M., Schmidt, M.J., 2010. Upper Devonian to Lower Mississippian conodont biostratigraphy of uppermost Wabamun Group and Palliser Formation to lowermost Banff and Lodgepole formations, southern Alberta and southeastern British Columbia, Canada: Implications for correlations and seq. *Bull. Can. Petrol. Geol.* 58, 295–341. <https://doi.org/10.2113/gscpgbull.58.4.295>.
- Kaiser, S.L., Aretz, M., Becker, R.T., 2016. The global Hangenberg Crisis (Devonian-Carboniferous transition): Review of a first-order mass extinction. *Geol. Soc. Spec. Publ.* 423, 387–437. <https://doi.org/10.1144/SP423.9>.
- Kendall, B., Reinhard, C.T., Lyons, T.W., Kaufman, A.J., Poulton, S.W., Anbar, A.D., 2010. Pervasive oxygenation along late Archaean ocean margins. *Nat. Geosci.* 3, 647–652. <https://doi.org/10.1038/ngeo942>.
- Klinkhammer, G.P., Palmer, M.R., 1991. Uranium in the oceans: where it goes and why. *Geochim. Cosmochim. Acta* 55, 1799–1806. [https://doi.org/10.1016/0016-7037\(91\)90024-Y](https://doi.org/10.1016/0016-7037(91)90024-Y).
- Kumpan, T., Kalvoda, J., Bábek, O., Holá, M., Kanický, V., 2019. Tracing paleoredox conditions across the Devonian–Carboniferous boundary event: a case study from carbonate dominated settings of Belgium, the Czech Republic, and northern France. *Sediment. Geol.* 380, 143–157. <https://doi.org/10.1016/j.sedgeo.2018.12.003>.
- Lampitt, R.S., Salter, I., Johns, D., 2009. Radiolaria: major exporters of organic carbon to the deep ocean. *Glob. Biogeochem. Cycles* 23, 1–9. <https://doi.org/10.1029/2008GB003221>.
- Love, L.G., 1971. Early diagenetic polyframboidal pyrite, primary and redeposited, from the Wenlockian Denbigh Grit Group, Conway, North Wales, U.K. *J. Sediment. Res.* 41, 1038–1044.
- Love, L.G., Vanguetaine, M., 1973. Polyframboidal pyrite of the Rochelival pyrite beds (Belgian Ardennes). *Ann. Geol. Soc. Belgium* 96, 347–360.
- Lyons, T.W., Severmann, S., 2006. A critical look at iron paleoredox proxies: New insights from modern euxinic marine basins. *Geochim. Cosmochim. Acta* 70, 5698–5722. <https://doi.org/10.1016/j.gca.2006.08.021>.
- McLennan, S.M., 2001. Relationships between the trace element composition of sedimentary rocks and upper continental crust. *Geochim. Geophys. Geosyst.* 2, 1021. <https://doi.org/10.1029/2000GC000109>.
- Morford, J.L., Emerson, S., 1999. The geochemistry of redox sensitive trace metals in sediments. *Geochim. Cosmochim. Acta* 63, 1735–1750. [https://doi.org/10.1016/S0016-7037\(99\)00126-X](https://doi.org/10.1016/S0016-7037(99)00126-X).
- Myrow, P.M., Hanson, A., Phelps, A.S., Creveling, J.R., Strauss, J.V., Fike, D.A., Ripperdan, R.L., 2013. Latest Devonian (Famennian) global events in western Laurentia: Variations in the carbon isotopic record linked to diagenetic alteration below regionally extensive unconformities. *Palaeogeogr. Palaeoclimatol. Palaeoecol.* 386, 194–209. <https://doi.org/10.1016/j.palaeo.2013.05.021>.
- Nameroff, T.J., Balistreri, L.S., Murray, J.W., 2002. Suboxic trace metal geochemistry in the eastern tropical North Pacific. *Geochim. Cosmochim. Acta* 66, 1139–1158. [https://doi.org/10.1016/S0016-7037\(01\)00843-2](https://doi.org/10.1016/S0016-7037(01)00843-2).
- Over, D.J., 2021. The Devonian-Carboniferous boundary in the United States. *Palaeobiodiv. Palaeoenvir.* 101, 529–540. <https://doi.org/10.1007/s12549-020-00428-1>.
- Partin, C.A., Bekker, A., Planavsky, N.J., Scott, C.T., Gill, B.C., Li, C., Podkovyrov, V., Maslov, A., Konhauser, K.O., Lalonde, S.V., Love, G.D., Poulton, S.W., Lyons, T.W., 2013. Large-scale fluctuations in Precambrian atmospheric and oceanic oxygen levels from the record of U in shales. *Earth Planet. Sci. Lett.* 369–370, 284–293. <https://doi.org/10.1016/j.epsl.2013.03.031>.
- Petrash, D.A., Gueneli, N., Brocks, J.J., Mendez-Dot, J.A., González-Arismendi, G., Poulton, S.W., Konhauser, K.O., 2016. Black shale deposition and early diagenetic dolomite cementation during oceanic anoxic event 1: the Mid-Cretaceous Maracaibo Platform, northwestern South America. *Am. J. Sci.* 316, 669–711. <https://doi.org/10.2475/07.2016.03>.
- Petty, D.M., 2019. An alternative interpretation for the origin of black shale in the Bakken Formation of the Williston Basin. *Bull. Can. Petrol. Geol.* 67, 47–69.
- Poulton, S.W., 2021. The iron speciation paleoredox proxy. In: *Cambridge Elements: Geochemical Tracers in Earth System Science*. <https://doi.org/10.1017/9781108847148>.
- Poulton, S.W., Canfield, D.E., 2005. Development of a sequential extraction procedure for iron: Implications for iron partitioning in continentally derived particulates. *Chem. Geol.* 214, 209–221. <https://doi.org/10.1016/j.chemgeo.2004.09.003>.
- Poulton, S.W., Canfield, D.E., 2011. Ferruginous conditions: a dominant feature of the ocean through Earth’s history. *Elements* 7, 107–112. <https://doi.org/10.2113/gselements.7.2.107>.
- Poulton, S.W., Raiswell, R., 2002. The low-temperature geochemical cycle of iron: From continental fluxes to marine sediment deposition. *Am. J. Sci.* 302, 774–805. <https://doi.org/10.2475/ajs.302.9.774>.
- Poulton, S.W., Fralick, P.W., Canfield, D.E., 2004. The transition to a sulphidic ocean ~1.84 billion years ago. *Nature* 431, 173–177. <https://doi.org/10.1038/nature02912>.
- Raasch, G.O., 1956. Late Devonian and/or Mississippian faunal succession in Stettler Area, Alberta. *Alberta Soc. Pet. Geol.* 4, 112–118.
- Raiswell, R., Canfield, D.E., 1998. Sources of iron for pyrite formation in marine sediments. *Am. J. Sci.* 298, 219–245. <https://doi.org/10.2475/ajs.298.3.219>.
- Raiswell, R., Newton, R., Wignall, P.B., 2001. An indicator of water-column anoxia: resolution of biofacies variations in the kimmeridge clay (upper Jurassic, U.K.). *J. Sediment. Res.* 71, 286–294. <https://doi.org/10.1306/070300710286>.
- Richard, B.C., Ross, G.M., Utting, H., 2002. U-Pb geochronology, lithostratigraphy and biostratigraphy of tuff in the upper Famennian to Tournaisian Exshaw Formation: evidence for a mid-Paleozoic magmatic arc on the northwestern margin of North America. *Can. Soc. Petrol. Geol. Mem.* 19, 158–207.
- Richards, B.C., Higgins, A.C., 1988. Devonian-Carboniferous boundary beds of the Palliser and Exshaw formations at Jura Creek, Rocky Mountains, southwestern Alberta. *Can. Soc. Petrol. Geol. Mem.* 14, 399–412.
- Richards, B.C., Bamber, E.W., Henderson, C.M., Higgins, A.C., Johnstone, D.I., Mamet, B. L., Meijer-Drees, N.C., 1994. Uppermost Devonian (Famennian) and Lower

- Carboniferous (Tournaisian) at Jura Ceek and Mount Rundle, southwestern Alberta. *Geol. Surv. Canada Open File 2866* (79 pp).
- Root, K.G., 2001. Devonian Antler fold and thrust belt and foreland basin development in the southern Canadian Cordillera: Implications for the Western Canada Sedimentary Basin. *Bull. Can. Petrol. Geol.* 49, 7–36. <https://doi.org/10.2113/49.1.7>.
- Ruttenberg, K.C., Berner, R.A., 1993. Authigenic apatite formation and burial in sediments from non-upwelling, continental margin environments. *Geochim. Cosmochim. Acta* 57, 991–1007. [https://doi.org/10.1016/0016-7037\(93\)90035-U](https://doi.org/10.1016/0016-7037(93)90035-U).
- Sageman, B.B., Murphy, A.E., Werne, J.P., Ver Straeten, C.A., Hollander, D.J., Lyons, T.W., 2003. A tale of shales: the relative roles of production, decomposition, and dilution in the accumulation of organic-rich strata, Middle-Upper Devonian, Appalachian basin. *Chem. Geol.* 195, 229–273. [https://doi.org/10.1016/S0009-2541\(02\)00397-2](https://doi.org/10.1016/S0009-2541(02)00397-2).
- Sandberg, C.A., Morrow, J.R., Ziegler, W., 2002. Late Devonian sea-level changes, catastrophic events, and mass extinctions. *Spec. Pap. Geol. Soc. Am.* 356, 473–487. <https://doi.org/10.1130/0-8137-2356-6.473>.
- Savoy, L.E., 1992. Environmental record of Devonian-Mississippian carbonate and low-oxygen facies transitions, southernmost Canadian Rocky Mountains and northwesternmost Montana. *Geol. Soc. Am. Bull.* 104, 1412–1432. [https://doi.org/10.1130/0016-7606\(1992\)104<1412:ERODMC>2.3.CO;2](https://doi.org/10.1130/0016-7606(1992)104<1412:ERODMC>2.3.CO;2).
- Savoy, L.E., Harris, A.G., Mountjoy, E.W., 1999. Extension of lithofacies and conodont biofacies models of Late Devonian to Early Carboniferous carbonate ramp and black shale systems, southern Canadian Rocky Mountains. *Can. J. Earth Sci.* 36, 1281–1298. <https://doi.org/10.1139/cjes-36-8-1281>.
- Schieber, J., Baird, G., 2001. On the origin and significance of pyrite spheres in Devonian black shales of North America. *J. Sediment. Res.* 71, 155–166.
- Schobben, M., Foster, W.J., Sleveland, A.R.N., Zuchuat, V., Svensen, H.H., Planke, S., Bond, D.P.G., Marcellis, F., Newton, R.J., Wignall, P.B., Poulton, S.W., 2020. A nutrient control on marine anoxia during the end-Permian mass extinction. *Nat. Geosci.* 13, 640–646. <https://doi.org/10.1038/s41561-020-0622-1>.
- Scott, C., Slack, J.F., Kelley, K.D., 2017. The hyper-enrichment of V and Zn in black shales of the Late Devonian-Early Mississippian Bakken Formation (USA). *Chem. Geol.* 452, 24–33. <https://doi.org/10.1016/j.chemgeol.2017.01.026>.
- Selby, D., Creaser, R.A., 2005. Direct radiometric dating of the Devonian-Mississippian time-scale boundary using the Re-Os black shale geochronometer. *Geology* 33, 545–548. <https://doi.org/10.1130/G21324.1>.
- Slomp, C.P., Epping, E.H.G., Helder, W., Van Raaphorst, W., 1996. A key role for iron-bound phosphorus in authigenic apatite formation in North Atlantic continental platform sediments. *J. Mar. Res.* 54, 1179–1205. <https://doi.org/10.1357/0022240963213745>.
- Smith, M.G., Bustin, R.M., 1998. Production and preservation of organic matter during deposition of the Bakken Formation (Late Devonian and Early Mississippian), Williston Basin. *Palaeogeogr. Palaeoclimatol. Palaeoecol.* 142, 185–200. [https://doi.org/10.1016/S0031-0182\(98\)00063-7](https://doi.org/10.1016/S0031-0182(98)00063-7).
- Smith, M.G., Bustin, R.M., 2000. Late Devonian and Early Mississippian Bakken and Exshaw black shale source rocks, Western Canada sedimentary basin: A sequence stratigraphic interpretation. *Am. Assoc. Pet. Geol. Bull.* 84, 940–960. <https://doi.org/10.1306/a9673b76-1738-11d7-8645000102c1865d>.
- Smith, M.G., Bustin, R.M., Caplan, M.L., 1995. Sequence stratigraphy of the Bakken and Exshaw formations: A continuum of black shale formations in the Western Canada Sedimentary Basin. *Seventh Int. Willist. Basin Symp.* 399–409.
- Sundby, B., Gobeil, C., Silverberg, N., Mucci, A., 1992. The phosphorus cycle in coastal marine sediments. *Limnol. Oceanogr.* 37, 1129–1145. <https://doi.org/10.4319/lo.1992.37.6.1129>.
- Tribouillard, N., Algeo, T.J., Baudin, F., Riboulleau, A., 2012. Analysis of marine environmental conditions based on molybdenum-uranium covariation—Applications to Mesozoic paleoceanography. *Chem. Geol.* 324–325, 46–58. <https://doi.org/10.1016/j.chemgeo.2011.09.009>.
- Van Cappellen, P., Qiu, L., 1997. Biogenic silica dissolution in sediments of the Southern Ocean. II. Kinetics. *Deep. Res. Part II Top. Stud. Oceanogr.* 44, 1129–1149. [https://doi.org/10.1016/S0967-0645\(96\)00112-9](https://doi.org/10.1016/S0967-0645(96)00112-9).
- Van Cappellen, P., Dixit, S., van Beuskom, J., 2002. Biogenic silica dissolution in the oceans: reconciling experimental and field-based dissolution rates. *Glob. Biogeochem. Cycles* 16, 1075. <https://doi.org/10.1029/2001gb001431>.
- Walliser, O.H., 1996. Global events in the Devonian and Carboniferous. In: Walliser, O.H. (Ed.), *Global Events and Event Stratigraphy in the Phanerozoic: Results of the International Interdisciplinary Cooperation in the IGCP-Project 216 'Global Biological Events in Earth History'*. Springer Berlin Heidelberg, pp. 225–250. https://doi.org/10.1007/978-3-642-79634-0_11.
- Webster, R.L., 1984. Petroleum source rocks and stratigraphy of Bakken Formation in North Dakota: Abstract. *Am. Assoc. Pet. Geol. Bull.* 68, 953. <https://doi.org/10.1306/AD46166F-16F7-11D7-8645000102C1865D>.
- Wei, H., Wei, X., Qiu, Z., Song, H., Shi, G., 2016. Redox conditions across the G–L boundary in South China: Evidence from pyrite morphology and sulfur isotopic compositions. *Chem. Geol.* 440, 1–14. <https://doi.org/10.1016/j.chemgeo.2016.07.009>.
- Wignall, P.B., Newton, R., 1998. Pyrite framboid diameter as a measure of oxygen deficiency in ancient mudrocks. *Am. J. Sci.* 298, 537–552. <https://doi.org/10.2475/ajs.298.7.537>.
- Wignall, P.B., Bond, D.P.G., Kuwahara, K., Kakuwa, Y., Newton, R.J., Poulton, S.W., 2010. An 80 million year oceanic redox history from Permian to Jurassic pelagic sediments of the Mino-Tamba terrane, SW Japan, and the origin of four mass extinctions. *Glob. Planet. Chang.* 71, 109–123. <https://doi.org/10.1016/j.gloplacha.2010.01.022>.
- Wilkin, R.T., Arthur, M.A., 2001. Variations in pyrite texture, sulfur isotope composition, and iron systematics in the black sea: Evidence for late Pleistocene to Holocene excursions of the O₂-H₂S redox transition. *Geochim. Cosmochim. Acta* 65, 1399–1416. [https://doi.org/10.1016/S0016-7037\(01\)00552-X](https://doi.org/10.1016/S0016-7037(01)00552-X).
- Wilkin, R.T., Barnes, H.L., 1997. Formation processes of framboidal pyrite. *Geochim. Cosmochim. Acta* 61, 323–339. [https://doi.org/10.1016/S0016-7037\(96\)00320-1](https://doi.org/10.1016/S0016-7037(96)00320-1).
- Wilkin, R.T., Barnes, H.L., Brantley, S.L., 1996. The size distribution of framboidal pyrite in modern sediments. *Geochim. Cosmochim. Acta* 60, 3897–3912. [https://doi.org/10.1016/0016-7037\(96\)00209-8](https://doi.org/10.1016/0016-7037(96)00209-8).
- Wilmens, M., 2000. Evolution and demise of a mid-Cretaceous carbonate shelf: the Altamira Limestones (Cenomanian) of northern Cantabria (Spain). *Sediment. Geol.* 133, 195–226.
- Zegeye, A., Bonneville, S., Benning, L.G., Sturm, A., Fowle, D.A., Jones, C.A., Canfield, D.E., Ruby, C., MacLean, L.C., Nomosatryo, S., Crowe, S.A., Poulton, S.W., 2012. Green rust formation controls nutrient availability in a ferruginous water column. *Geology* 40, 599–602. <https://doi.org/10.1130/G32959.1>.
- Zhang, F., Dahl, T.W., Lenton, T.M., Luo, G., Shen, S., Zhong, Algeo, T.J., Planavsky, N., Liu, J., Cui, Y., Qie, W., Romaniello, S.J., Anbar, A.D., 2020. Extensive marine anoxia associated with the Late Devonian Hangenberg Crisis. *Earth Planet. Sci. Lett.* 533, 115976. <https://doi.org/10.1016/j.epsl.2019.115976>.